Transition Metal Modified Zinc Oxide for Spintronics

thesis submitted towards the partial fulfillment of the requirements for the award of the degree of

Master of Technology
In
Materials & Metallurgical Engineering

Submitted by

SUNITA MEHTA

ROLL. No. 600802023

Under the supervision of

Dr. K.K. RAINA

Deputy Director & Distinguished Professor (SPMS)

Thapar University, Patiala

School of Physics and Material Science

THAPAR UNIVERSITY,

PATIALA – 147004,

INDIA

July, 2010

BONAFIDE CERTIFICATE

I hereby certify that the work which is being presented in the thesis entitled *"TRANSITION METAL MODIFIED ZINC OXIDE FOR SPINTRONICS"* is an authentic record of my own work carried out in the partial fulfilment of the requirements for the award of the degree of Master of Technology in Material science and Metallurgical Engineering under the supervision of Dr. K.K.Raina, Deputy Director and Distinguished Professor, School of Physics and Material Science, Thapar University, Patiala during January to June 2010.

This is to be certified that the above statement made by the candidate is correct and true to the best of my knowledge and belief.

(Dr. K.K.Raina)

Deputy Director& Distinguished Professor

SPMS, Thapar University

Patiala-147004

Countersigned by:

27/7/10

Dr. O.P. Pandey

Professor & Head

SPMS,Thapar University

Patiala, Punjab

27/7/10

Dr. R.K.Sharma

Dean, Academic Affairs

Thapar University

Patiala, Punjab

ACKNOWLEDGEMENT

It takes a lot of hard work and austere discipline to really make the things happening. I am indebted to all the people who provided the assistance, encouragement and cooperation to complete my work.

I would like to express my sincere gratitude to my esteemed and worthy supervisor **Dr. K.K.Raina, Deputy Director & Distinguished Professor, School of Physics and Materials Science, Thapar University** *for his insight help, guidance, effective supervision and encouragement in carrying out this dream come true. His wide knowledge and his logical way of thinking have been of great value for me.*

I am deeply grateful to **Dr. O.P. Pandey, Professor & Head, School of Physics and Material Science** *for his detailed and constructive comments, and for his important support throughout this work. His ideas and concepts made a remarkable influence on my career in the field of material science.*

I warmly thank **Dr. Kulvir singh, Associate Professor, School of Physics and Material Science** *for their kind support, guidance and untiring help during my difficult moments.I am also thankful to* **Dr. S.D.Tiwari, Dr. D.P.Singh, Dr. Loveleen Brar** *and all the faculty members of School of Physics and Materials Science for their constructive Suggestions at different stages of this work.*

It gives me immense pleasure to express my special thanks to **Mr. Ravi Shukla** *(Ph.D Scholar) who always take keen interest in guiding me during my work.*

I am extremely Thankful to **Dr. Ratnamala Chatterjee,** *Professor, IIT Delhi and* **Dr.H.Bhunia***, Assistant Professor, Department of Chemical Engineering, Thapar University, without whom the work would not have been possible. I would also like to thank* ***Mr. Purshottam Singh*** *for their great support.*

I wish my heartfelt thanks to research scholars **Shikha Kapila Neeraj Sharma, Pratibha Singh, Parveen Paliwal, Renu Dahiya, Rekha Gandhi, Pankaj Kumar** *for their generous help and good wishes.*

I am also thankful to all the staff members of the School of Physics and Materials Science for their full co-operation, motivation and generous support. I would also like to thank my friends **Ishan Choudhary, Sumit Bhardwaj, Pankaj Chamoli, Rashmi Mittal** *who stand with me in every situation. Without them, this work would not have been accomplished .*

I have no words to express thanks to my ***Parents*** *who always a constant inspiration for me and supporting me spiritually throughout my life.*

Above all I render my gratitude to the ***ALMIGHTY*** *who bestowed self-confidence, ability and strength in me to complete this work.*

(**Sunita Mehta)**

Abstract

In the present study, an attempt has been made to synthesize pure and 3d-transition metal doped (up to 5%) ZnO using chemical route (Co-precipitation method) in the basic medium. Synthesized samples were characterized using XRD, FTIR, UV-Visible Spectrophotometer, SEM and SQUID in order to understand structural, chemical, optical, morphological and magnetic behaviour of these samples. XRD analysis gives information about the successful doping up to 5%, as no impurity peak has been seen in any case and all the samples exhibit wurtzite hexagonal structure with average particle size 7 -26 nm. FTIR spectra reveal the formation of Zn-O bond as we observed the reflection at 452.798 cm^{-1}in all synthesized pure and doped systems. Optical studies inferring that the addition of Ni, Co and Mn decreased the optical band-gap. SEM images do not give any significant information, as the clumps of spherical particles have been observed in these synthesized samples. Magnetic measurements indicate that Ni doped samples exhibit both diamagnetic and ferromagnetic character, later being more dominant. However, Co and Mn doped system exhibit only ferromagnetic behaviour. Such ferromagnetic behaviour is new to the field with Ni and Mn (5%) doping.

Contents

List of figures

List of tables

CHAPTER -1

INTRODUCTION

1.1 PREAMBLE

The fast growing field of microelectronics and information processing has been based on fabricating devices out of conductors and doped semiconductors, where the charge of the electron is exploited. Generation to generation improvements in the performance of microelectronic devices is accomplished by shrinking the size of the elements in the chips. For decades, Information Technology (IT) industry has followed Moore's Law, that the number of transistors on a chip doubles about every two years, but conventional solid state electronics may soon reach a limit due to the increasing heat dissipation challenges of charge current and quantum size effects in small devices[1]. Similarly, information storage, the second vital piece of the microelectronic revolution, depends on magnetic storage devices that exploit the spin component of the electron. Here, continued performance gains are bumping up against the superparamagnetic limit associated with nanosized features. An alternative approach for improving the performance of future devices would be to make the individual components multifunctional. The fabrication of devices, where both of the charge and spin functionalities of the carrier were combined, could revolutionize the technology by providing new device designs and architectures that could potentially boost performance, reduce power consumption, and introduce new features (e.g. instantaneous boot up and data retention in the power-down state). This branch of electronics, which involves utilizing both the spin and charge of the electron, is commonly referred to as **spintronics**[2]. Therefore, in pursuit of more efficient, higher performance, and lower power-consuming devices like FETs, LED_S, MRAM, etc research is now being conducted that is focussed on the complementary use of the charge and spin components of the electron, as it might be applied to information storage and processing.

Spintronics is an exciting and rapidly expanding field of microelectronics and nanoelectronics. All spintronic devices act according to the simple scheme: (1) information is stored (written) into spins as a particular spin orientation (up or down), (2) the spins, being attached to mobile electrons, carry the information along a wire, and (3) the information is read at a terminal. Spin orientation of conduction electrons survives for a

relatively long time (nanoseconds, compared to tens of femtoseconds during which electron momentum decays), which makes spintronic devices particularly attractive for memory storage and magnetic sensors applications, and, potentially for quantum computing where electron spin would represent a bit (called qubit) of information.

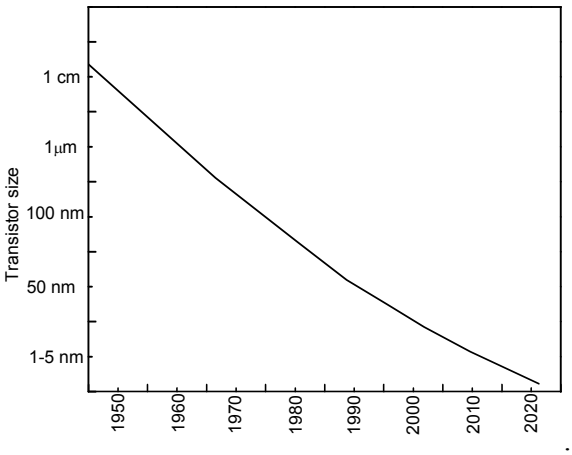

Figure 1.1: Moore's law

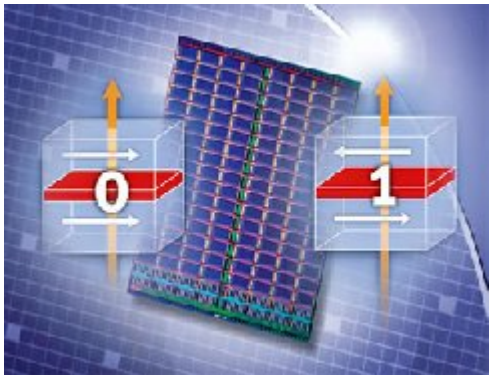

Figure 1.2: Schematic showing how information is stored into spins depending upon their orientation

It was the discovery of **Giant Magnetoresistance** (GMR) in the early 1980s by **Peter Grunberg** and **Albert Fert**, that initiated spintronic research and resulted in the first generation of a spintronic device in the form of the spin valve[3]. Basically, GMR Effect is the change in the resistance of the material, when the relative orientation of the metallic layers in the system is changed from antiparallel to parallel configuration, by applying a magnetic field. Since, this change in resistance is much larger (greater than 50%) than expected for normal magnetoresistance, therefore this effect became known as Giant magnetoresistance. Figure 1.3 shows the spin valve structure and figure 1.4 shows GMR read head using this spin valve structure.

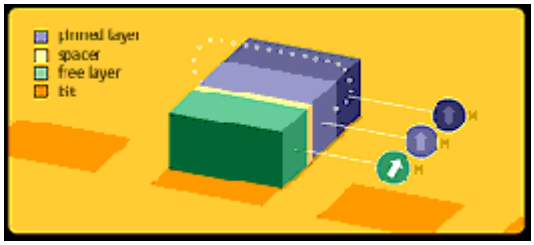

Figure 1.3: spin valve

figure 1.4: GMR read Head

The origin of the effect lies in the spin dependent transmission of conduction electrons between the magnetic layers through the nonmagnetic spacer, which depends on the relative orientation of the moments of the magnetic layers

Today, spintronic devices are ubiquitous on the desktop as spin valve play their role as the active element in the read head of most hard disk storage devices.GMR was followed rapidly by the discovery of tunnelling magnetoresistance leading to the magnetic tunnel junction that has been utilized in developing the next generation of memory known as magnetic random access memory-an example of another spintronic device.

Second generation spintronic devices will integrate magnetic materials and semiconductor devices to create new flexible devices such as spin transistors and spin logic. These second generation spintronic devices will not just improve the existing capabilities of electronic transistors, but will have new functionalities enabling future computers to run faster, but consume less power, and have the potential to revolutionize the IT industry as did the development of the transistor 50 years ago.

1.2 MATERIALS FOR SPINTRONICS

Early work has been focussed on finding suitable host materials that display ferro-magnetic properties at room temperature and identifying workable approaches to the efficient injection, transport, detection and manipulation of spin polarized carriers. Most of the devices in spintronics made so far are based on metallic thin films. Ferromagnetic metallic films with metallic spacer layers show giant magnetoresistance and have been used in read heads in computer disk drives for several years. Ferromagnetic metals have several advantages for use in devices:

a) The transition temperatures are very well above room temperature.
b) The magnetic anisotropy can be tuned by alloying
c) The fabrication routes are well established

Since conventional semiconductors like Si and GaAs are diamagnetic and possess very small g-factor (a measure of the interaction strength with an applied magnetic field). However it is less easy to couple ferromagnetic metals to the conventional semiconductors because of the very large resistance mismatch. Thus the hunt is now on for a ferromagnetic semiconductor that could be integrated with standard semiconductor technology. It is anticipated that if ferromagnetism and electronics transport could be coupled in semiconductors, the effect of magnetism would be significantly stronger than the phenomena observed in metals. Within this field of research, **dilute magnetic**

semiconductors, also known as semimagnetic semiconductors, are especially important materials. In these materials, rare earth or transition metal ions replace a considerable number of the native ions in the semiconductor's lattice. This offers opportunities for a new generation of devices, combining standard microelectronics with spin dependent effects that arise from the interaction between the spin of the carrier and the magnetic properties of the material.

Figure 1.5 shows a schematic of DMS material. Here, the unpaired d electrons on the transition metal dopant ions would give rise to a magnetic moment. If these moments could be coupled ferromagnetically then a magnetically ordered DMS systems would be available that could be directly integrated with spin-based devices (e.g. LEDs and FETs) fabricated from the same host semiconductor.

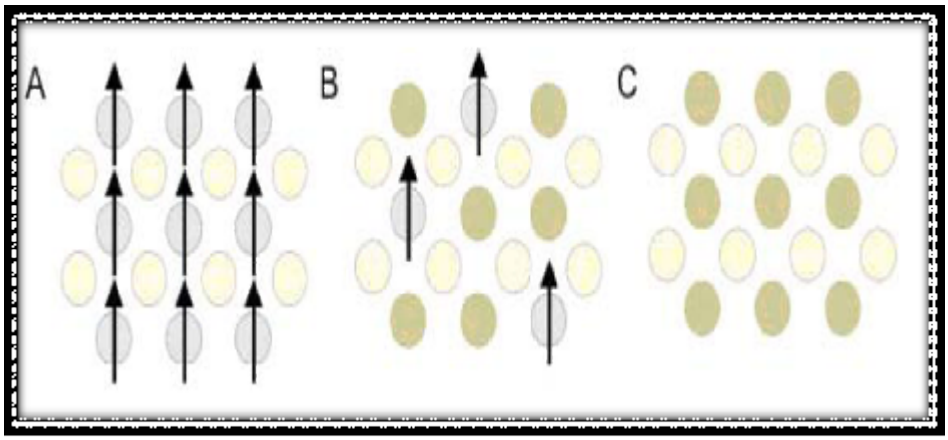

Figure 1.5: Schematic showing three types of materials a) Magnetic, b) Dilute magnetic Semiconductor and c) non magnetic semiconductor materials [4].

Several examples of ferromagnetic semiconductor materials are e.g.:

- Manganese-doped Indium Arsenide and Gallium Arsenide (GaMnAs), with Curie temperature around 50–100 K and 100–200 K, respectively
- Manganese-doped Indium Antimonide, which becomes ferromagnetic even at room temperature and even with less than 1% Mn.
- Oxide semiconductors
    - Manganese- and iron-doped indium oxide, ferromagnetic at room temperature
    - Manganese-doped zinc oxide
    - n-type Cobalt-doped zinc oxide

- Titanium dioxide:
  - Cobalt-doped titanium dioxide (both rutile and anatase), ferromagnetic above 400 K
  - Chromium-doped rutile, ferromagnetic above 400 K
  - Iron-doped rutile and iron-doped anatase, ferromagnetic at room temperature
  - Nickel-doped anatase
- Manganese-doped tin dioxide, with Curie temperature at 340 K
- Iron-doped tin dioxide, with Curie temperature at 340 K
- Carbon doped Zinc Oxide
- Zero gap materials like HgTe, HgSe

Generally, The II-VI semiconductors are favoured over III-V semiconductors because of their high solid solubility of transition metal atoms. As in ZnO, the thermal solubility of 3d-transition metals is larger than 10 mol% and the electron effective mass is as large as 0.3 m_e, therefore the amount of injected spins and carriers will be large, thus making transition metal doped ZnO ideal for the fabrication of spintronics devices[5]. Moreover ZnO is a well-known piezoelectric and electro-optic material and therefore the incorporation of ferromagnetism in ZnO can lead to a variety of new multifunctional phenomena.

1.3 ZnO- A NOVEL SEMICONDUCTOR

Of all diluted magnetic semiconducters and oxides, ZnO has aroused the most interest because of its attractive properties. The Wurtzite ZnO has great prospects in optoelectronic applications due to its direct wide band gap (E_g ~ 3.3 eV). The wide band gap of ZnO makes it transparent in the visible range which is maintained even at very high carrier concentrations, where ZnO shows metallic conductivity, making ZnO a promising material to be used as a transparent conductor. The advantage it has over other wide band gap semiconductors, is its large exciton binding energy (~60 meV) .Since this value is more than twice of room temperature thermal energy (k_BT= 25 meV), it will lead to an intense near-band-edge excitonic emission above room temperature[5]. Room temperature Hall mobility of the order of 200 $cm^2V^{-1}s^{-1}$ and carrier concentration up to ~ 10^{21} cm^{-3} can be achieved by group III substitutional doping of ZnO[6]. These favourable electrical and

optical properties allow ZnO to have wide applications such as transparent electrodes in flat panel displays and solar cells, thin film gas sensor, varistor, surface acoustic wave (SAW) devices, optical wave-guides, ultraviolet LASER source, and ultraviolet detectors[7]. The biggest roadblock in processing of a fully ZnO – based device is the unavailability of highly p-type conducting ZnO. Although a number of groups have tried to address this issue by using various growth methods and doping with various group V elements (N, P, As and Sb), reproducible and reliable high p-type conductivity in ZnO is yet to be achieved. Apart from all these attractive properties, the high solubility of the various 3d transition elements in ZnO adds further to its advantage to be used in spintronics application, as higher concentrations of magnetic dopants can be introduced in it without precipitating out as secondary phases or metallic nanoclusters[8].

1.3.1 Crystal Structure

ZnO crystallizes in three different forms:

a) Wurtzite (hexagonal) structure

b) Zinc blende

c) Rock salt (NaCl) structure.

Wurtzite is thermodynamically the most stable state under ambient conditions, although the other two structures also appear under specific conditions. The zinc – blende state is stable only when grown on cubic substrates and the rock salt structure can be obtained only at very high pressures. Some of the other interesting semiconductors which crystallize in the same wurtzite structure are GaN, ZnSe, ZnTe, etc. The wurtzite structure has a hexagonal close packed (hcp) bravais lattice and belongs to the $P6_3mc$ space group. The ZnO structure consists of two interpenetrating hcp sublattices of cation (Zn) and anion (O) which are displaced along the c-axis by the Zn – O bond length. Figure 1.5 shows a schematic of the wurtzite structure. The lattice constants of ZnO are: a = 3.252 A^0 and c = 5.215 A^0, which gives a c/a ratio ~ 1.603. This departure from a c/a value of 1.633 for an ideal hcp structure is primarily due to the electronegativities between Zn^{2+} and O^{2-} ions. The presence of defects such as oxygen vacancies, Zn interstistials, impurities and dislocations have also been know to affect the variation in lattice parameters[6].

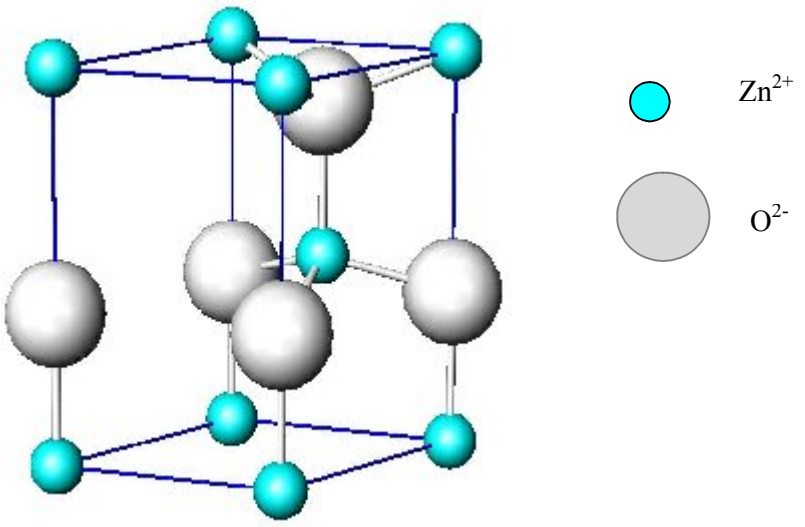

Figure 1.6: Schematic of Wurtzite crystal structure

1.3.2 Electronic Band Structure

A very important property of any given semiconductor is its band structure, because many important properties such as the band gap and effective electron and hole masses are derived from it. ZnO is considered most suitable semiconductor among all his family members for ultraviolet lasing at room temperature, device application as well as possibilities to engineer the band gap. So a clear understanding of the band structure is important to explain the electrical properties and many other phenomena.Experimental methods to determine the band structure normally involve measurements by UV and X-ray reflection/absorption/ emission techniques, photoelectron spectroscopy (PES) and Angular resolved Photoelectron spectroscopy (ARPES)[6] .These methods basically measure the energy difference by inducing transitions between different electronic levels (for example, transitions from the upper valence-band states to the upper conduction states, and the lower valence-band states).

Local density approximation (LDA) and density functional theory (DFT) are the most extensively used computational techniques to calculate the band structure of ZnO[9]. The valence band extends down to about 10 eV below the Fermi level. The deepest valence band is mainly the O3s orbital, whereas, the upper valence band is composed of Zn 3d, 4s, 4p and O2p orbitals. The conduction band consists of Zn4s, 4p and O2p orbitals. Figure 1.7 shows total density of states for ZnO.

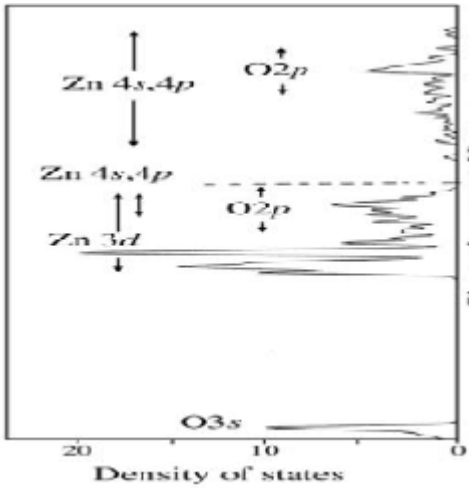

Figure 1.7: Density of states of ZnO[9]

1.3.3 Effect of native defects and dopants

The effect of doping and presence of native defects on the electrical and magnetic properties of ZnO can be well understood by analysis of the electronic band structure. The energy levels of various dopants and defects can affect the DOS in conduction or valence bands or in the mid-gap. If the DOS of the energy levels defects or dopants are delocalized and overlap with the conduction or valence bands, then they might contribute to improving conduction whereas for those having localized DOS in the mid-gap might lead to increase in resistance by compensation effects. The energy levels of the 3d orbitals of the transition metal dopants and their interactions with the energy states of ZnO and native defects play an important role in determining the magnetic ordering in the TM doped ZnO DMS. The electronic band structure of the host semiconductor and the DOS of the energy states of dopants also determine the mechanism governing the ferromagnetic ordering:- either free carrier mediated or via localized electrons associated with native defects.

ZnO is inherently n-type. The main reason for the n-type conductivity has been proposed to be a native defect, either O vacancies or Zn interstitials, acting as a shallow donor, although the role played by either of these two defects in the origin on n-type conductivity in pure ZnO is still controversial. Usually these point defects appear in crystals as Schottky (pair of anion and cation vacancy) or Frenkel (vacancy – interstitial pair of the same ion). Theoretical calculations by Bin et al.[10] showed that mid-gap states are formed by the introduction of defects such as V_O, V_{Zn}, O_i and Zn_i. By performing numerous studies on optical and electrical properties of ZnO and on the diffusion process, Krueger[11]

estimated the energy levels of these native defects in ZnO, which is shown schematically in Figure 1.7. V_O and V_{Zn} have been assigned as the dominant donor and acceptor, respectively. In oxygen rich conditions Zn vacancies (V_{Zn}) will dominate where as, under Zn rich or oxygen deficient conditions, O vacancies (V_O) will dominate. From the theoretical calculations, it has been predicted that the energy of formation for V_O is lower than that of Zn_i and hence gives rise to n-type conductivity. In the Figure 1.8, Zn vacancies are represented as V_{Zn}' and V_{Zn} ". Zn_i^x and Zn_i^* represent Zn interstitials and Oxygen vacancies are denoted by $V_O{}^x$ and $V_O{}^*$.

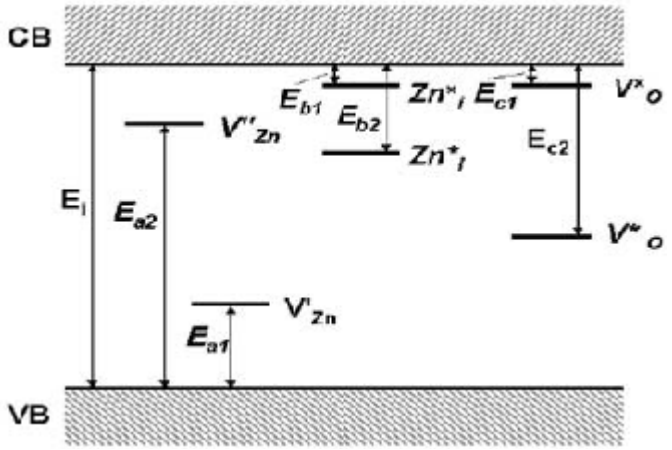

Figure 1.7: Electronic energy levels of native defects in ZnO[11]

The activation energy for the two acceptor levels of V_{Zn}' and V_{Zn}" are given by E_{a1} = 0.7 x 10^{-4} eV and E_{a2} = 2.8 x 10^{-3}eV, respectively. The binding energies for the two Zn interstitial donor levels are given by E_{b1} = 0.05 eV and E_{b2} = 0.5 x 1.5 x10^{-4} eV. The binding energies for the two donor levels of the oxygen vacancies is given by E_{c1} = 0.05 eV and E_{c2} = 2.6x10^{-4} eV. Thus it was seen that both V_o and Zn_i can act as shallow donors but there is a great debate about which one is the dominant donor defect responsible for n-type conductivity. With the incorporation of dopants, the situation becomes even more interesting. The formation of complexes between defects themselves and with other dopant impurities can not be ruled out. With recent reports of native defects, especially shallow donors like Zn interstitials and Oxygen vacancies, playing an important role in determining the magnetic ordering in ZnO DMSs, the understanding of interaction between the defect energy states and the transition metal 3d orbitals becomes even more necessary.

Some of the basic physical parameters of ZnO can be compiled as given in the table 1.1

Table 1.1: Basic physical properties of ZnO[12]

Property	Value
Density(g/cc)	5.606
Bond Length(μm)	1.977
Melting Point(^{0}C)	1975^{0}C
Thermal Conductivity($WK^{-1}m^{-1}$)	0.6 , 1-1.2
Static Dielectric Constant	8.656
Refractive Index	2.008, 2.029
Energy Gap(eV)	3.4
Exciton Binding Energy(MeV)	60
Heat Capacity(cal/mol K)	9.6
Youngs modulus (GPa)	111.2± 4.7

CHAPTER-2

DILUTE MAGNETIC SEMICONDUCTORS

2.1 ZINC OXIDE BASED DILUTE MAGNETIC SEMICONDUCTORS

Attractive optical and electrical properties of ZnO coupled with Dietl's prediction that p type Zn(Mn)O would be ferromagnetic at room temperature, made it a prospective candidate for spintronic applications[13.]The high solubility of the various 3d transition elements in ZnO adds further to its advantage over the III-V semiconductors as higher concentrations of magnetic dopants can be introduced without precipitating them out into secondary phases or metallic nanoclusters.

The reason[2] why the prediction was made for p doping was that the interaction between magnetic d electrons on the manganese and the oxygen p electrons in the valence band was known to be much stronger than their interaction with the s electrons in the conduction band. It is necessary to have unequal filling of the magnetically split band to stabilize ferromagnetism, also following extensive work on GaMnAs, which is of the p type.

The experimental situation, however, is controversial, because there are numerous experimental reports both on the presence and the absence of ferromagnetism in ZnO (the case of Mn-doped samples is particularly controversial) flanked by theoretical controversies on the nature of the ferromagnetism of ZnO DMS.

According to Dietl's prediction, the Curie temperature of Mn doped p-type wide band gap semiconductors should be a function of both hole density and concentration of magnetic dopants. Thus high values of hole density and magnetic dopant concentration are necessary to obtain a high Tc. While n-type ZnO with high carrier concentrations has been realized, p-type doping has been difficult to achieve[6.] Hence, according to Dietl's predictions it would be difficult to achieve high temperature ferromagnetism in Mn doped ZnO since high hole density is not achieved by p-type doping. Ab initio calculations based on local density approximations by Sato and Katayama-Yoshida also predicted that hole mediation is necessary for ferromagnetic ordering in Mn doped ZnO[14.] However for ZnO doped with other transition metals like V, Cr, Fe, Co and Ni, ferromagnetic ordering was predicted without any additional carriers[15]. The same authors predicted (using calculations by KKR method in coherent-potential approximation) that ferromagnetic ordering in Fe, Co and Ni doped ZnO is stabilized by introduction of additional electrons.

2.2 MECHANISMS OPERATIVE IN DMS MATERIALS

In spite of the experimental success achieved in realizing ferromagnetism above room temperature in a number of DMS systems, a fundamental understanding of the origin of ferromagnetism is still far from clear. There exist some theoretical models which have sought to explain the observed ferromagnetism in these systems. We briefly discuss a few important exchange mechanisms:

2.2.1 Carrier–induced interaction and RKKY exchange

A free carrier induced interaction called RKKY exchange, proposed simultaneously by Rudderman, Kittel, Kasuya and Yoshida,[18-20] can explain ferromagnetic exchange between spins in n-type doped materials. This mechanism is based on coupling of localized d-spins of the magnetic ions by means of an interaction through the conduction electrons. Of special interest here is the Zener mean field theory proposed by Dietl[21] which is based on the original Zener theory and the RKKY interaction. There are three possible types of magnetic interactions:

i. Direct exchange between d-shells of the neighbouring atoms, resulting in the following energy term :

$$E_{direct} = \tfrac{1}{2}\, \alpha\, S_{d1}.S_{d2}$$

Where, S_d is the net moment on each ion and α is always positive, but its magnitude is proportional to the wave function overlap.

ii. Exchange due to coupling between the conduction electrons and the inner d electrons.

The energy resulting due to this interaction is given by :

$$E = -\beta S_d.S_c$$

where, S_c is the net magnetization of the conduction electrons and β is always positive.

iii. The last coupling energy is due to the Fermi kinetic energy of the electrons. This

is given by :

$$E_{kinetic} = \frac{1}{2} \gamma S_c$$

where, $\gamma = 2\varepsilon / 3n$, and ε is the kinetic energy at the top of the Fermi distribution and n is the number of conduction electron per atom.

The conditions for ferromagnetic and antiferromagnetic behaviour are as follows :

$$\beta^2 > \alpha\gamma \rightarrow \textbf{Ferromagnetism}$$

and

$$\beta^2 < \alpha\gamma \rightarrow \textbf{Antiferromagnetism}$$

The ferromagnetism will be achieved in all systems for which above equation is satisfied, i.e. where the neighbouring incomplete d shells are sufficiently separated from each other such that the indirect ferromagnetic coupling mediated by the conduction electrons dominate over the direct antiferromagnetic coupling. The 2nd term is of most importance and forms the bulk of the interaction in the RKKY mechanism. This term envisages an indirect exchange coupling of atomic magnetic moments by conduction electrons. This interaction is characterized by a coupling coefficient, J, given by :

$$\mathbf{J(R_i - R_j) = 9\pi(J_0^2/E_F)F(2k_F \left| R_i - R_j \right|)}$$

where, k_F is the radius of the conduction electron Fermi surface, R_s is the lattice position of the point moment, E_F is the Fermi energy and

$$F(x) = \frac{x\cos x - \sin x}{x^4}$$

The RKKY exchange integral, J, oscillates from positive to negative values. Hence depending upon the separation between two ions, their moments are coupled either ferromagnetically or antiferromagnetically.

2.2.2 Double – exchange interaction

The double-exchange mechanism is a theory that predicts the relative ease with which an electron may be exchanged between two species. Hopping of the electron over the d states is facilitated if the electrons do not have to change spin direction in order to accommodate the Hund's rules. In this mechanism, magnetic ions in different charge states couple with each other by virtual hopping of the 'extra' electron from one ion to the other. In the DMS material, if neighboring TM magnetic moments are in the same direction, the TM-*d* band is widened by the hybridization between the up-spin states as shown in the figure 2.1. Therefore, in the ferromagnetic configuration the band energy can be lowered by introducing carriers in the *d* band. In these cases, the 3*d* electron in the *partially* occupied 3*d*-orbitals of the TM is allowed to hop to the 3*d*-orbitals of the neighboring TM, if neighbouring TM ions have parallel magnetic moments. As a result, the *d*-electron lowers its kinetic energy by hopping in the ferromagnetic state. This is the so-called double exchange mechanism. In such systems, spin ordering is always accompanied by a large increase in conductivity which leads to effects like colossal magneto resistance. This mechanism is typically present in mixed valence manganites like (La,Sr)MnO3 , where hopping of the electron between the Mn^{3+} and Mn^{4+} levels stabilizes the ferromagnetic state.

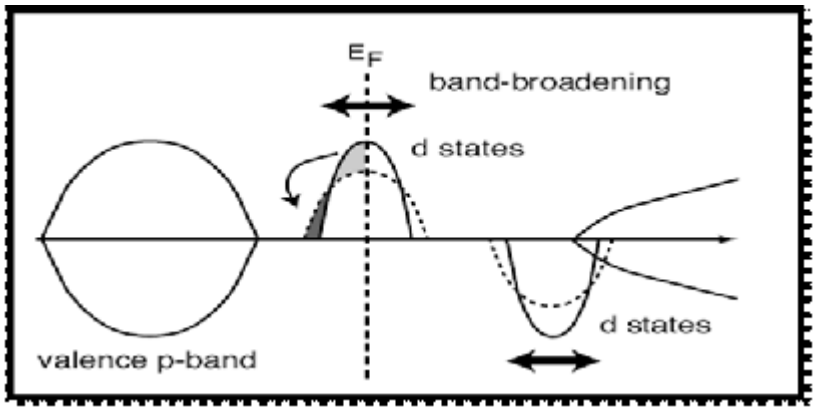

Figure 2.1: Double exchange mechanism

Although Sato and Katayama –Yoshida[14] in their theoretical study of ferromagnetism in transition metal doped ZnO suggested that the origin of ferromagnetism in DMSs was the double exchange mechanism based on Akai's work [22], However, this is not believed to be the case for two main reasons. Firstly this is a nearest neighbour interaction and would rule

out long-range ferromagnetic ordering that is essential for high temperature ferromagnetism. Secondly there is no evidence of mixed valency commonly occurring in DMSs.

2.2.3 Super exchange interaction

Super exchange is the magnetic coupling of nearest neighbour cations via an intermediatory non magnetic anion (for e.g O^{2-} in case of oxides). Due to the sp-d exchange interaction, electrons from the negative anion are donated to the vacant d orbitals of the magnetic ion. These electrons couple with the localized spins of the magnetic ions leading to an antiferomagnetic interaction between the spins of neighbouring magnetic ions. Since the Superexchange is predominantly antiferromagnetic and short ranged, it also cannot account for the long range ferromagnetic ordering seen in transition metal doped DMSs. But as the dopant concentration approaches the percolation threshold associated with the nearest neighbour cation coupling, antiferromagnetic coupling between nearest neighbour cations does start occurring and this reduces the average magnetic moment per dopant ion.

2.2.4 Bound Magnetic Polaron Model

Recent reports of high temperature ferromagnetism in low carrier density systems suggest that the mechanism for long-range ferromagnetic ordering cannot be explained just by the mediation through free carriers. Also the short-ranged exchange interactions like double exchange or super exchange can not explain such long-range ferromagnetic ordering at very low magnetic ion concentrations. A defect mediated mechanism like bound magnetic polaron exchange model (fig 2.2) can explain the long-range ferromagnetic ordering in such systems.

The bound magnetic polarons are formed due to the exchange interaction of localized holes (vacancies) with magnetic impurities. And in this model, spins of many transition-metal ions get aligned with that of much lower number of weakly bound carriers such as excitons within a polaron radius.

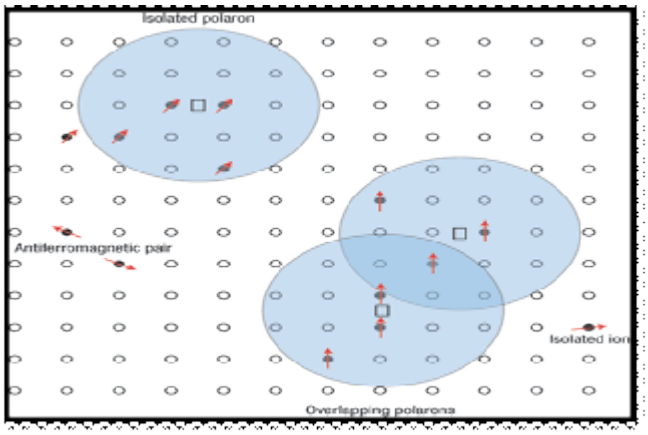

Figure 2.2 : Schematic of Bound Magnetic Polarons : A donor electron couple with its spin antiparallel to impurities with a 3d shell that is half or more than half full lying within its hydrogenic orbit. Cation sites are represented by small circles,oxygen is not shown and the unoccupied oxygen sites are represented as squares[23]

To understand the physics of this phenomenon, one may consider two neighbouring polarons (Fig. 2.3). The localized holes of these polarons both act on the impurities surrounding them thus producing an effective magnetic field for these impurities. The energy minimum is reached by this system when the impurity spins are parallel to this effective field, and the magnitude of the field is maximum. The maximum of this effective magnetic field is achieved when the spins of the localized holes are parallel. Therefore at low temperatures the system should eventually reach the state where the spins of all holes point in the same direction, and all impurity spins point in the same or in the opposite direction, depending on the sign of the impurity-hole exchange interaction.

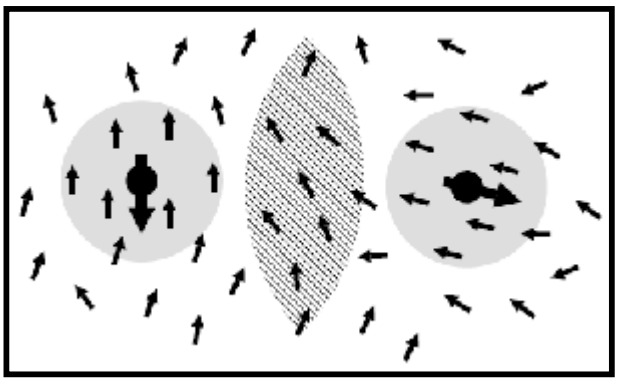

Figure 2.3: Interaction of two bound magnetic polarons. The polarons are shown with gray circles; small and large arrows show impurity and hole spins, respectively[23]

The neighbouring magnetic polarons overlap and interact via magnetic impurities forming correlated clusters of polarons. One observes a ferromagnetic transition when the size of such clusters is equal to the size of the sample. This model is inherently attractive for low carrier density systems such as many of the electronic oxides. The polaron model is applicable to both *p*- and *n*-type host materials. Even though the direct exchange interaction of the localized holes is antiferromagnetic, the interaction between bound magnetic polarons may be ferromagnetic for sufficiently large concentrations of magnetic impurities. This enables ferromagnetic ordering of the Mn ions in an otherwise insulating or semi-insulating material.

2.2.5 Donor-Impurity Band Exchange Model

This model suggests that the origins of the magnetic behaviour may not be related to interactions between intrinsically pure material. Instead, the defect centers are essential for mediating ferromagnetism in the materials. Thus, it is not the pure bulk material which leads to an overall ferromagnetic behaviour, but rather the defects and interfaces play a crucial role in determining the overall magnetic behaviour of the system. In this case, the magnetic interaction is also mediated through the percolation of bound magnetic polarons, which in this case are centered on a donor. For ZnO, this donor has been suggested to be an oxygen vacancy defect, i.e. an f-center. Thus, in order to achieve a strong long-range magnetic interaction, it is essential to have an adequate number of vacancies, as well as a sufficient carrier concentration, such that ferromagnetic percolation may take place. This approach seems to have some evidence in the oxide based materials, unusual ferromagnetic interaction observed in copper-containing materials. Figure 2.4 shows a schematic of the band splitting induced by this model.

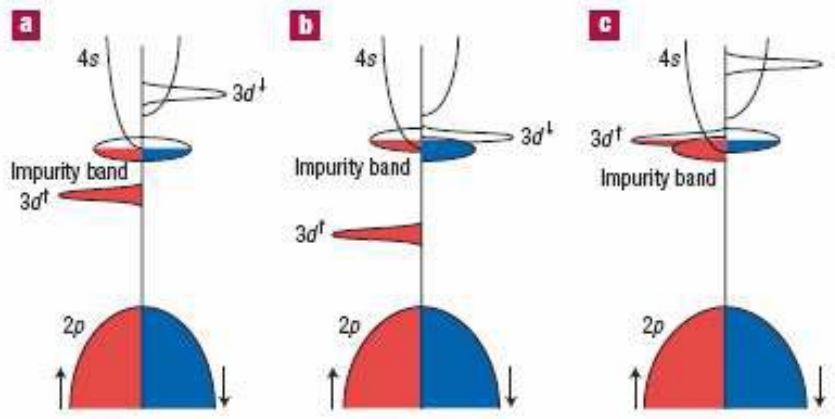

Figure 2.4: Schematic of effective overlap between the impurity band 3d energy states .Here there are shown three different possible impurity band alignments. The first would lead to comparatively low temperature ferromagnetism, whereas the latter two would result in high temperature ferromagnetism[23].

2.3 POTENTIAL DEVICE APPLICATIONS

Achievement of high temperature T_c in ZnO based DMS systems will facilitate the development of multifunctional spintronic devices where the electron spin, along with the charge, can be exploited to both process and store information. The low flipping energy of a spin compared to charge allows it to be easily manipulated by application of external magnetc fields. A longer coherence or relaxation time, on the order of nanoseconds compared to femtoseconds for charge of the electrons, allows the spin to persist much longer than the charge of the electrons, which are destroyed by scattering or recombination. Thus combining spin functionality of the electron along with its charge in devices will not only add multifunctionality to the microelectronic devices, but would make the new generation devices much smaller, faster, less power consuming and more robust than the existing devices. But in order to have practical device applications utilizing the spin of electrons it is necessary to have efficient injection, transfer and detection of spin across a semiconductor at room temperature. Injection of spin polarized carriers across a ferromagnetic metal-semiconductor interface has been found to yield very low injection efficiencies due to scattering due to defects and resistance mismatch across the interface. Hence achievement of ferromagnetism in a diluted magnetic semiconductor holds much promise for efficient spin injection into semiconductors for use in spintronic devices. some possible spintronic device applications are:

2.3.1 Magnetic memory devices

The first spintronic device application of economic impact came into being following the discovery of the "Giant Magneto Resistance" (GMR) effect[24]. When the magnetic moments of the two ferromagnetic layers separated by a non-ferromagnetic layer are aligned in the same direction, the resistance across the stack is low, when aligned in opposite directions the resistance is high due to interfacial scattering. Such a layer system is known as a "spin valve" where one of the ferromagnetic layers is pinned, but the moment of the other layer is free to easily align with an applied magnetic field, as shown in the figure 2.5.

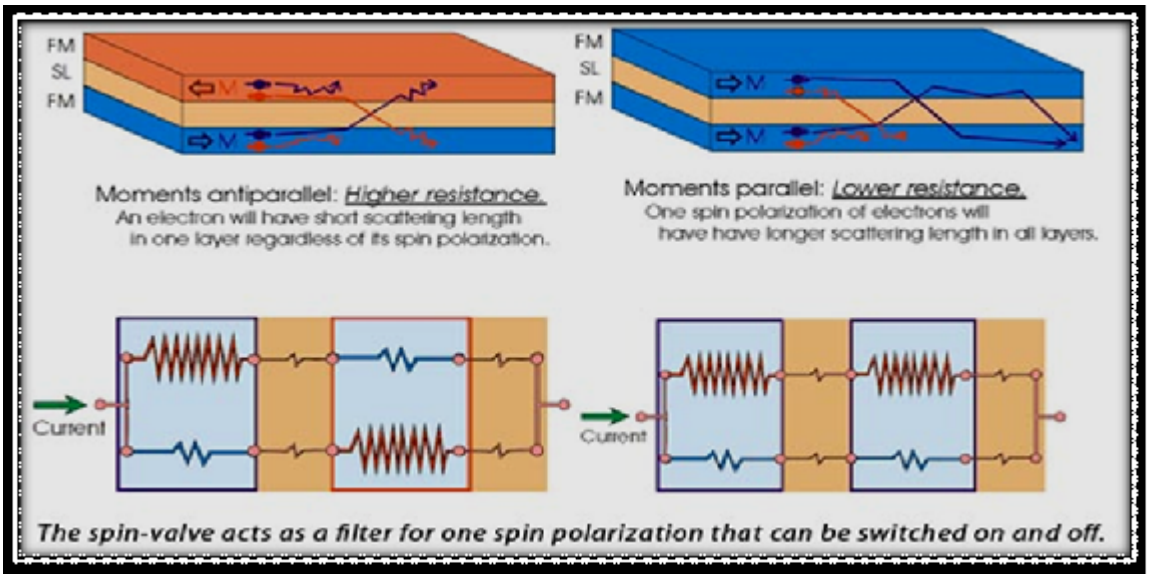

Figure 2.5 : Spin Valve structure showing change in resistance

Magnetic read heads used in magnetic disc recorders must sense very small magnetic fields. Hence, the recent switch to GMR read head technology has lead to a 10 fold increase in the magnetic storage capacity from 1 to 20 Gigabits [25]. IBM was the first to launch GMR reads in the market in 1997(Figure 1). By flipping the spins in one layer, the spin valve also acts as a switch. Thus, information can be stored as "0" and "1" (magnetization between layers being anti-parallel or parallel) just like in semiconductor RAM (Random Access memory). The advantage, magnetic random access memory (MRAM) will have over their semiconductor counterparts, is that they are non-volatile in

nature, smaller, faster, consume less power and be much more robust in conditions of high temperature and high-level interference.

2.3.2 Spin-FET

Datta et al.[26] were the first to propose the idea of a Spin FET device (Figure 2.6). They proposed that current modulation due to spin-orbit coupling can be achieved in a small band gap semiconductor FET having a spin polarizing (ferromagnetic metal or DMS) source and drain electrode. In this device a spin polarizing electrode (source or polarizer) preferentially injects spin polarized carriers into the channel that is then collected by another polarized electrode (drain or analyzer). Its operation is very similar to that of a conventional charge based FET. The relative orientation of the electron spins in the channel and the source and drain moments determines the current, it being maximum when they are all aligned. In the spin-FET, an interaction between the electric field and the spin precession of the carriers by the Rashba spin-orbit coupling effect[27] occurs when a relatively low gate voltage is applied. The current can be effectively shut off if this interaction is strong enough to turn the spin orientation of the carriers out of alignment with the drain contact. This can take place at a bias voltage that is much lower than that required to shut off the current in a charge controlled FET. A ZnO based spin-FET was proposed by Sato and Katayama-Yoshida[28].

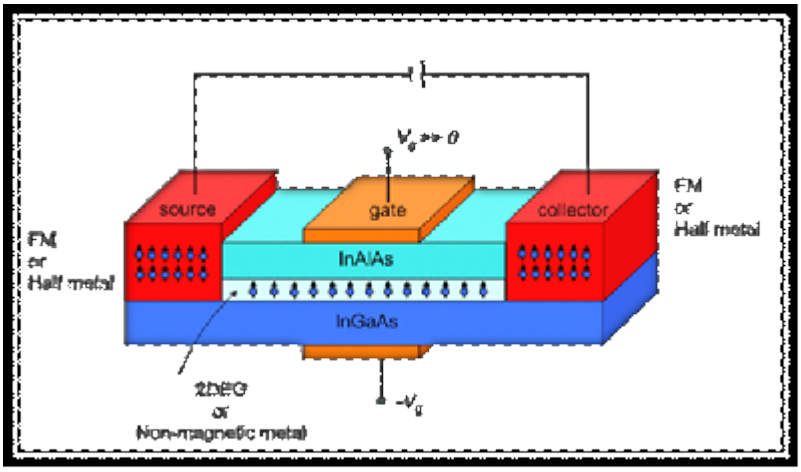

Figure 2.6: Spin FET

2.3.3 Spin-LED

Circularly polarized light is emitted by a spin-LED after the recombination of spin polarized charge carriers which are electrically injected into a semiconductor heterostructure. Such a device structure will allow modulation of the polarization of the light emitted by the spin-LED by applying an external magnetic field. Emission of spin polarized light has been shown in II-VI semiconductors and the III-As. A straightforward approach of attaining spin-polarized light emission will be to dope the top contact p-GaAs layer of the GaAs/InGaAs LED structure with Mn . A schematic of such a device is shown in Figure 2.7.

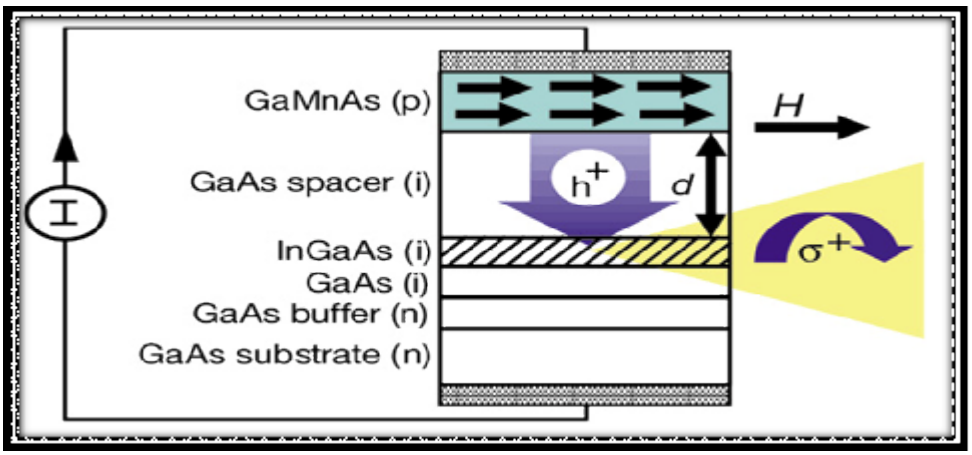

Figure 2.7: Schematic of a Spin-LED showing Injection of spin-polarized holes into a light-emitting *p-n* diode using a ferromagnetic semiconductor (Ga,Mn)As

2.4 LITERATURE REVIEW

The earliest reports in the field of DMS date back to the 1960s. Extensive research was done on Eu- and Cr-based chalcogenides (e.g EuSe, EuS, EuO, CdCr2Se4, and CdCr2S4)[29]. However, these systems proved to be very difficult to grow and possessed very low Curie temperatures, thereby limiting their practical applications.

In 1970s and 80s ,Studies on the broad class of II-VI compounds continued [30]. It was found that materials systems like CdTe, CdSe, HgTe, ZnSe, ZnTe, etc could be substitutionally doped with Mn and can be made DMS.

In 1989,the first thin film DMS was reported by Munekata et al.[31]. They studied Mn doped InAs films grown by low temperature MBE in the temperature range of 200-300^{0}C. These films had n-type conductivity. Films grown at 200^{0}C were homogenous and were found to

be paramagnetic, while films grown at 300^0C showed ferromagnetic behaviour. However, the ferromagnetism was attributed to the presence of MnAs nanoclusters.

In 1992 Ohno et al. conducted magneto-transport studies on p-type InMnAs thin films epitaxially grown by low temperature MBE [32].

In 1996 Ohno et al.[33] reported for the first time the growth of GaMnAs DMS thin films. This was of particular interest since GaAs was a well studied system that was widely used for optoelectronic applications. The Curie temperature was found to be ~ 60 K for a Mn concentration of 5%.

Then in 1998 Ohno reported ferromagnetism above 100 K in p-type GaMnAs[4]. Unfortunately, to date, the highest reported value of Tc for Mn doped GaAs is 172 K by Nazmul et al.[34].The low Curie temperature hinders its use as practical material system for use in spintronic applications. Thus, the search for other host semiconductor systems that would have ferromagnetism at temperatures above room temperature continued.

A major advance in this search was achieved with the theoretical work of Dietl et al. [35]. They used the Zener model [36] of ferromagnetism to predict Curie temperatures for transition metal doping of some widely used wide band gap semiconductors. Figure 2.6 shows calculated Tc values for different semiconductors. The most promising are found to be GaN and ZnO doped with 5% Mn, which showed Tc above 300 K.

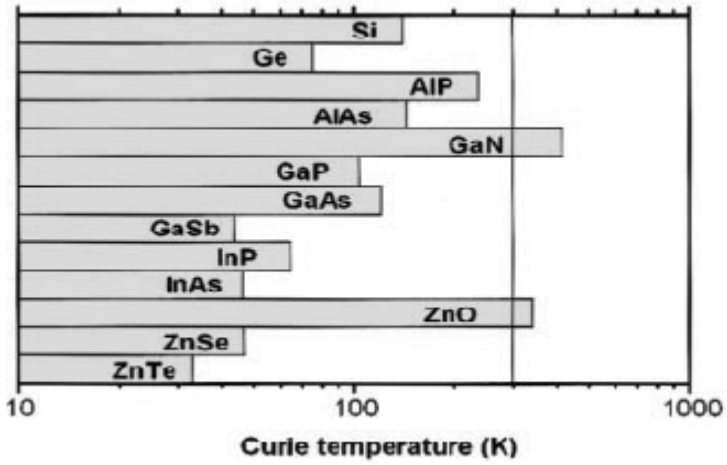

Figure 2.8: Predicted Curie Temperatures of Mn-doped Wide Band gap Semiconductors

In 2001, The first observation of room temperature ferromagnetism was reported by Reed et al.[37] in GaMnN thin films grown by metal-organic chemical vapour deposition

Soon thereafter, Ueda et al.[38] examined the n-type $Zn_{1-x}M_xO$(x=0.05-0.25) system (M= Co, Mn, Cr and Ni) grown by pulsed laser deposition (PLD), and reported that only the Co-doped films displayed ferromagnetism above room temperature. They found that very high carrier (electron) concentrations of 10^{20} cm^{-3} were required.

In 2002, Mizokawa et al.[39] examined the electronic structure of the oxide-diluted magnetic semiconductor $Zn_{1-x}Mn_xO$.basically the electronic structure of the substituted 3d transition metal impurities in semiconductors is influenced by two competing factors: strong 3d-host hybridization and strong 3d-3d coulomb interactions. The strong coulomb interactions between the 3d electrons is responsible for the multiplet structures observed in d-d optical absorption spectra. On the other hand, the hybridization between the transition metal 3d and the host valence band gives rise to the magnetic interaction between the localized 3d spins and the carrier in the host valence band.A configuration-interaction approach using a cluster model was used in this paper.In the cluster model electronic-structure parameters can be estimated by analyzing core-level and valence band photoemmision spectra of DMS.By using the obtained parameters as input, it is possible to estimate the magnitude of the magnetic interaction between the localized 3d spins and the carriers.The present CI calculations predict that the p-d exchange constant in $Zn_{1-x}Mn_xO$ is -2.7eV and that its magnitude is much larger than that in $Ga_{1-x}Mn_xAs$.

In 2003, A.S.Risbud et al.[40] presented results of the preparation,characterization and detailed computation of polycrystalline ZnO with upto 15% substitution of the zinc sites by divalent Cobalt. The experimental results indicate the dominant magnetic interaction in well-characterized stoichiometric phases $Zn_{1-x}Co_xO$, x=0.05, 0.10, 0.15, is nearest neighbour antiferromagnetic. Computations suggest that robust ferromagnetism will only occur in the presence of additional hole doping.

In the same year, Norton et al.[41] investigated the magnetic properties of Mn-implanted n-type ZnO single crystals that are codoped with Sn. As a 4^+ valence cation, Sn should behave as a doubly ionized donor, this introducing states deep in the gap. Conduction from the deep donors is due to impurity band and/or hopping conduction, as opposed to conventional free electrons excited to the conduction band. Hysterisis was clearly observed in magnetization versus field curves.

Then, P.Sharma et al.[42] reported ferromagnetism above room temperature in Mn doped ZnO prepared by solid state route as well as in thin films prepared by pulsed laser

deposition technique. The unique feature of sample preparation was low temperature processing. It was found that when the temperature was above 700^0 C, samples exhibit clustering and were not ferromagnetic at room temperature.

In 2004, B.B.Liu et al.[43] studied structure and magnetic properties of Co-doped ZnO prepared by Sol-gel method.Ferromagnetic properties at room temperature were observed with the coercive field about 90Oe.but the origin of ferromagnetism was not known.
Further in the same year, Jung H.Park et al.[44] investigated the origin of ferromagnetism in ZnO based systems by using Co-doped ZnO thin films .It was found that $Zn_{1-x}Co_xO$ thin films were paramagnetic for $x<0.12$. On the other hand, films with x greater than 0.12 were characterized by the Co-metal clustering and apparently showed room-temperature ferromagnetism.
In spite of all the above observations, Absence of ferromagnetism in Mn- and Co-doped ZnO was then reported by **C.N.R.Rao et al.**[45] the year 2005.They suggested that it can be achieved only by doing co-doping with some additional charge carriers.

Then, Subhash Thota et al.[17] also done the magnetic studies of transition metal (Ni, Co,Mn) containing ZnO powders.Observation of hysterisis loops fo Ni doped ZnO confirms its ferromagnetic state. Whereas the magnetic behaviour of manganese and cobalt doped ZnO is however different namely, (i) no hysteresis loops, (ii) decrease in magnetization with increase of Mn or Co content, and (iii) identical *M–T* curves under ZFC and FC conditions. The inverse susceptibility versus temperature curves of Zn1−*x*Mn*x*O compounds reveal ferrimagnetism with N´eel temperature *T*N of 4 K for x = 0.02, but antiferromagnetism for x = 0.15 and 0.25 with Curie–Weiss temperature of −43 and −30 K, respectively.
After that, following the C.N.R.Rao conclusion, the concept of codoping was introduced. N.H.Hong et al.[46] studied the role of Cu, which is co-doped in $Zn_{1-x}Mn_xO$ thin films.It was found that the codoping with Cu enhanced the magnetic moment for some extent in some specific cases,but not very crucially as theories have predicted.

Further kittilstved et al.[47] by some chemical manipulation, reported that ferromagnetism in Co-doped ZnO can be stabilized by n-type defects. Whereas, p-type defects can stabilize ferromagnetism in Mn-doped ZnO.

Whereas Sluiter et al.[48] identified a crucial role of defects in the observed weak and preparation sensitive ferromagnetism in ZnO:Mn and ZnO:Co. It was found that Co has the

best potential as a Zn substitutional dopant in ZnO for producing DMS when combined with a hole dopant such as Li_{Zn} or an electron dopant such as Cu_{Zn} or interstitial Zn.

In 2006, Sundarsan et al.[49] observed the ferromagnetism as a universal feature of nanoparticles of the otherwise nonmagnetic oxides such as CeO_2, Al_2O_3,ZnO,In_2O_3 and SnO_2 Conversely, the bulk samples obtained by sintering the nanoparticles at high temperatures became diamagnetic. As there were no magnetic impurities present, the origin of ferromagnetism was assumed to be due to the exchange interactions between localized electron spin moments resulting from oxygen vacancies at the surfaces of nanoparticles. Kanwalpreet Bhatti et al.[50] also observed the room temperature ferromagnetism in nanocrystalline ZnO:Co system.The recently proposed bound magnetic polaron model was reported to account for the observed ferromagnetic ordering. Further It was demonstrated experimentally by Liu et al.[51] that high temperature ferromagnetism in Co-doped ZnO can be obtained through increasing the carrier concentration which was realized by codoping of a few percent of Al.

Manivannan et al.[52] prepared the bulk samples of $Zn_{0.95}Co_{0.05}O$ and $Zn_{0.95}Mn_{0.05}O$ and reported the magnetic properties of these samples before and after annealing in 5%H_2/95% Ar at 573K for 6h.The as prepared samples were paramagnetic. Whereas after hydrogenation, the magnitude of Mn/ZnO was unchanged but Co/ZnO acquires room temperature ferromagnetism with a magnetic moment of $0.35\mu_B$/Co site and hysteresis loop with saturation magnetization Ms=1.2 emu/g. Deka et al.[53] observed the presence of Co metal after the reduction process which is the origin of room temperature ferromagnetism.

Jayakumar et al.[54] reported the magnetism in Mn-doped ZnO nanoparticles prepared by co-precipitation method. DC magnetization measurements showed ferromagnetic ordering above room temperature for 2 at% Mn-doped ZnO nanoparticles annealed at 675K.

In the year 2007, V.K.Sharma et al.[55] observed the room temperature ferromagnetism in Mn doped samples synthesized by solid state reaction as well as in those prepared by sol-gel method..However the samples synthesized by sol-gel method were found to have lower Tc values and also lower magnetization, which could be possibly due to the presence of any secondary phases in the samples, which generally shows antiferromagnetic interaction and responsible for the observed lowering of T_c and magnetization values. Further Ivill et al.[56] reported the enhanced magnetization in ZnO thin films co-doped with Mn and P. The result was consistent with hole-mediated ferromagnetism in Mn-doped ZnO.

Pearton et al.[57] also observed the room temperature ferromagnetism in Co-doped ZnO thin films grown by Pulsed Laser Deposition Technique.

Kanwal Preet Bhatti et al.[58] demonstrated the intrinsic and extrinsic origin of room temperature ferromagnetism in ZnO:Co system. It was found that upon vacuum annealing, the magnetization of the sample increases significantly and the sample remains ferromagnetic upto 630^0C.This was attributed due to the formation of cobalt clusters and thus the ferromagnetic ordering is extrinsic in nature. Further, On the subsequent air annealing of the vacuum annealed samples reverts back the magnetization to a value that was observed in the pristine air sintered sample. This was due to the complete oxidation of the cobalt clusters. Furthermore, the sample's magnetization at room temperature and also its temperature dependence upto 630^0C remain unaffected by further annealing in vacuum or air, a feature required of a material for its device applications. The curie temperature of the robust sample was ~450^0C.

Garcia et al.[59] showed experimentally that it is possible to induce room temperature like behaviour in ZnO nanoparticles without doping magnetic impurities but simply inducing an alteration of their electronic configuration by capping with some organic molecules.

In 2008, In order to shed some light on the origin of ferromagnetism, P.Sharma et al.[60] investigated the detailed atomic structure of (Co,Ga)-codoped ZnO experimentally as well as theoretically. Also above room temperature ferromagnetism in Co-doped ZnO nanoparticle powders were obtained by codoping with Ga. It is found that Co ions substitute Zn sites while Ga ions were located at octahedral interstitial sites together with one O vacancy. Electrons from the Ga $4p\uparrow$ states transform to the unfilled Co $3d\downarrow$ states. The strong hybridization between the charge carriers in the Co 3*d* and Ga 4*p* states and electronic polarization for surrounding O ions at Co ions are detected. Finally, the Ga-4*p* electrons merged with conduction band and polarized O ions act as medium for an indirect exchange between the Co ions, which could be the origin of ferromagnetism in the (Co, Ga) ZnO

In the year 2009, Gao et al.[61] reported the room temperature ferromagnetism of pure ZnO nanoparticles, which were prepared by coprecipitation method. Magnetization measurements indicated that the ZnO nanoparticles annealed in air at 450,550,650 and 800^0C exhibit the RTFM and decrease in the ferromagnetism is performed with the increase in annealed temperature.It was also found that the ferromagnetism of ZnO nanoparticles increases after annealing in vacuum condition and decreases after annealing in a rich oxygen atmosphere. These results confirmed that the oxygen vacancies play an important role in introducing ferromagnetism for the ZnO nanoparticles.

In the same year, Snure et al.[62] reported a detailed study aimed on understanding the origin of ferromagnetism in Ni-doped ZnO films. A pulsed laser deposition technique was used to deposit Ni-doped ZnO films on sapphire substrates under different oxygen pressures ranging from 10^{-6} to 0.1 Torr. A detailed structure-property correlation and analysis of the results revealed that the ferromagnetism in ZnO:Ni films is not an inherent property of the material but results due to a strong tendency of Ni to precipitate out in the ZnO matrix.

In April 2010, Shi et al.[63] observed that the Co-doped ZnO samples prepared by sol-gel and magnetron sputtering methods, exhibit different intrinsic magnetic properties, one being paramagnetic, while the other being ferromagnetic even at room temperature. By studying the different O *K*-edge XANES spectra obtained in $Zn_{1-x}Co_xO$ samples, it was revealed that the incorporation of the Zn interstitials in the lattice is crucial to the observation of high temperature ferromagnetism in Co-doped ZnO. Thus the defect engineering is of great importance in achieving room temperature ferromagnetism in ZnO.

Ye et. al.[64] have detected the intrinsic room temperature ferromagnetism over n-type carbon-doped ZnO prepared through solid-state reaction. The results of first- principle calculations based on density functional theory revealed that the CZn_4O_{12} unit is the origin of magnetic moment in the carbon –doped ZnO system.

Besides ZnO based materials, Wang et al.[65] have depicted zero-gap materials like solid solutions of $Pb_{1-x}Sn_xTe$, $Pb_{1-x}Sn_xSe$ and Bi_xSb_{1-x} for future Spintronics, electronics and optics.

Thus the nature of magnetism is strongly dependent on the method adopted for sample preparation and processing conditions such as temperature, pressure etc.

2.5 GAPS IN THE STUDY

- From the above literature survey, it is evident that lot of work has been done on the room temperature ferromagnetism in transition metal doped ZnO. But the real origin of ferromagnetism had not been known till today,which need more experimentation and investigation to understand the exact origin of ferromagnetism in such system and their use for technological applications.Further such systems can be tailored by varying the composition and the processing conditions,which may enhance the magnetic properties of the system.
- On the other hand,co-doping of transition metal on ZnO is the area needs to be probed as already discussed by C.N.R.Rao

2.6 OBJECTIVES

a) Synthesization and characterization of transition metal (Ni, Co, Mn) doped ZnO.

b) To study the magnetic properties of transition metal doped ZnO

c) To enhance the value of magnetization by co-doping with charge carriers like Al, Ga, P, Sb**.**

2.7 SIGNIFICANCE AND RELEVANCE OF STUDY

In the field of spintronics, it is essential to develop semiconductors with ferromagnetically polarized carriers at room temperature (RT) such that the spin as well as charge of the carriers can be coupled with an external magnetic field to control devices. Fascination toward the development of such materials is due to their tremendous application potential, which will have a huge effect on our day to day life. For example, such types of material will be capable of integrating the electronics, magnetism, and optical functionalities in a single material, leading to low cost, high-speed, and small sized devices operating at very low power.

CHAPTER-3

MATERIAL PREPARATION AND CHARACTERIZATION

3.1 METHODS FOR THE PREPARATION OF NANOPARTICLES:

Basically, There are two approaches for the synthesis of nanomaterials: viz top-down and bottom-up. Top down approach involves the breaking down of the bulk material into nano sized structures or particles. An example of such a technique is high-energy ball milling. The alternative approach, which has the potential of creating less waste and hence the more economical, is the 'bottom- up'. Bottom up approach refers to the build up of a material from the bottom: atom-by-atom, molecule-by-molecule, or cluster-by-cluster.

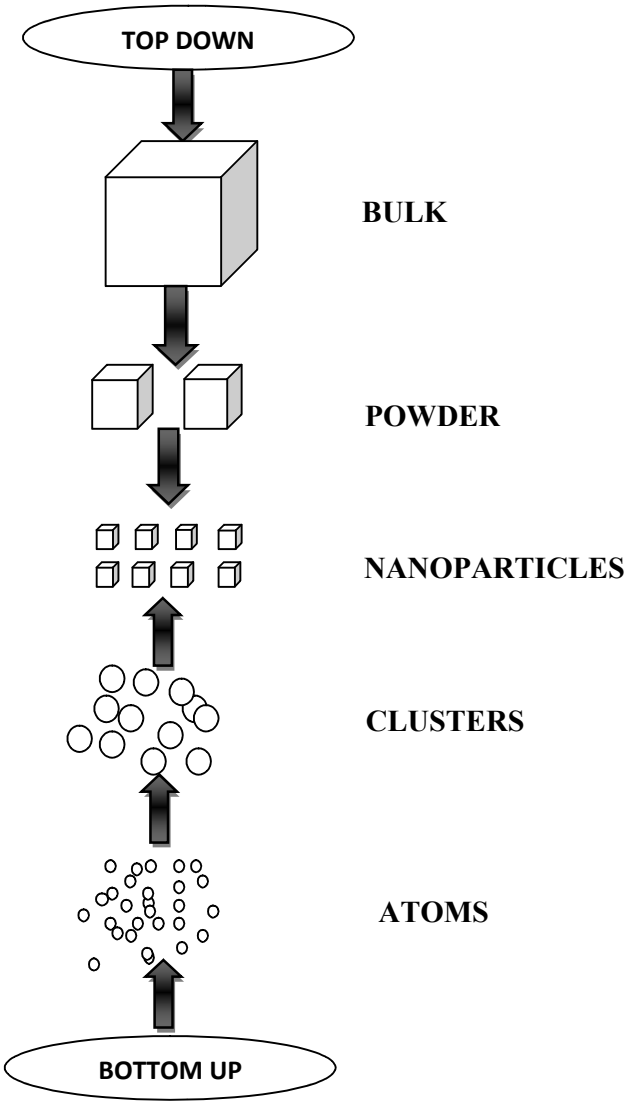

Figure 3.1: Schematic representation of the building up of Nanostructures

Further Top-down and Bottom-up approaches consist of the following methods:

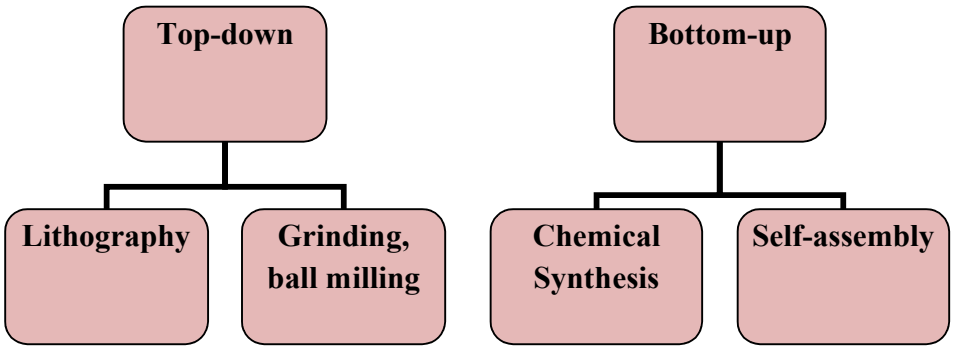

The chemical synthesis is one of the best and economic routes for the preparation of powdered samples. The chemical synthesis consists of many known methods which include co-precipitation method, Sol-Gel, SILAR, Spray Drying, Spray pyrolysis, Freeze drying etc.

Here, Novel **Co-precipitation method** has been used for the preparation of pure and doped samples. This method enables a high purity, low temperature synthesis, good chemical homogeneity and a narrow size distribution of the particles.

This method comprises of 2 stages:

a) Hydrolysis:

The precursors generally used are metal alkoxides having the general formula $M(OR)_Z$. Where, 'M' is metal and 'R' is alkyl group. These alkoxides are prepared by the reaction of metal with alcohol in which the hydroxide hydrogen is replaced by metal and therefore it is a metal-oxygen-carbon bond system.

$$\mathbf{M + z\,ROH \longrightarrow M(OR)_Z + z/2\,H_2} \quad \text{.....(1)}$$

The nature of alcohol has a significant effect on the reaction. Forexample, Sodium reacts vigorously with methanol and ethanol but the reaction is quite slow with isopropanol and extremely slow with tertiary butanol.

Now, during the hydrolysis reaction, water molecule interacts with the alkoxide and following an electronic arrangement, a molecule of alcohol is expelled out:

$$\mathbf{M(OR)_Z + H_2O \longrightarrow M(OH)(OR)_{Z-1} + ROH} \quad \text{.....(2)}$$

It should be noted down that in the presence of the excess water, metal alkoxide form

insoluble hydroxide or hydrated metal alkoxides depends upon metal for eg:

$$Al(OR)_3 + H_2O \longrightarrow AlO(OH)\downarrow + 3\,ROH \quad \text{.....(3)}$$

$$AlO(OH) + H_2O \longrightarrow Al(OH)_3\downarrow \quad \text{.....(4)}$$

The formation of insoluble precipitates as represented above makes it impossible polymerisation to occur. So it should be avoided

b) Condensation:

In the condensation reaction, the hydroxyl metal alkoxide product react further to form polymerizable species.

Condensation results in the formation of nanoscale clusters of metal oxides or hydroxides often with groups embedded or attached to them.

$$M(OR)_{Z-1}(OH) + M(OR)_{Z-1}(OH) \longrightarrow (OR)_{Z-1}MOM(OR)_{Z-1} + H_2O \text{ ……(3)}$$

$$M(OR)_{Z-1}(OH) + M(OR)_Z \longrightarrow (OR)_{Z-1}MOM(OR)_{Z-1} + ROH \text{ ……(4)}$$

The factors which have the severe effect on the reaction and the production of the suspension are listed below:

- pH (medium of the reaction)
- Temperature and time of reaction
- Reagent concentration
- Nature and concentration of catalyst
- [H_2O/M] molar ratio
- Aging temperature and time
- washing
- Drying

Moreover the reactivity of the metal atom is dependent largely on the extent of charge transfer and the ability to increase its co ordination number. As the electro negativity

decrease the ability to increase it's co-ordination number increases with their radii. The chemical reactivity of the corresponding alkoxides increases with their ionic radii.

3.2 EXPERIMENTS PERFORMED

3.2.1 Synthesis of pure ZnO :

The chemical used in the synthesis are:

Table 3.1: The list of chemicals used for the synthesis of pure ZnO

Chemical name	Company
Zinc acetae	**SDFCL**
Ethanol	**SDFCL**
Sodium Hydroxide(pellets)	**SDFCL**

The precursor materials employed for the particle synthesis were used as received without any purification. The molar ratio and amount of the materials used is shown in following table 3.2.

Table 3.2: The molar ratio and amount of materials used for synthesis of pure ZnO

Chemical Name	Chemical Formula	Moles required	Material Taken(g)
Zinc Acetate	$Zn(CH_3COO)_2.2H_2O$	0.01	2.197
Ethanol	CH_3CH_2OH	----	100 ml
Sodium Hydroxide (pellets)	NaOH	0.02	0.8

EXPERIMENTAL PROCEDURE:

- The glass wares (three neck round bottom flask, measuring cylinder, beaker) were cleaned and rinsed with distilled water and acetone and dried in vacuum oven over night.

- Zinc acetate and ethanol in required amounts were charged in round bottom flask and the solution was stirred gently for 2 hours at about 70^0C on hot plate.

- Sodium Hydroxide pellets were added to the solution in order to adjust the pH around 10.82 and again stirred for 2 hours at 70^0C. After that solution was allowed to cool to room temperature.

- The final product was washed with ethanol many times to make it free from the complex.
- After filtration, filtered sample was heated at 90^o C in oven for 2 hours. Finally sample was grinded and characterized using different techniques (XRD, FTIR, DTA,TGA,SQUID etc.).

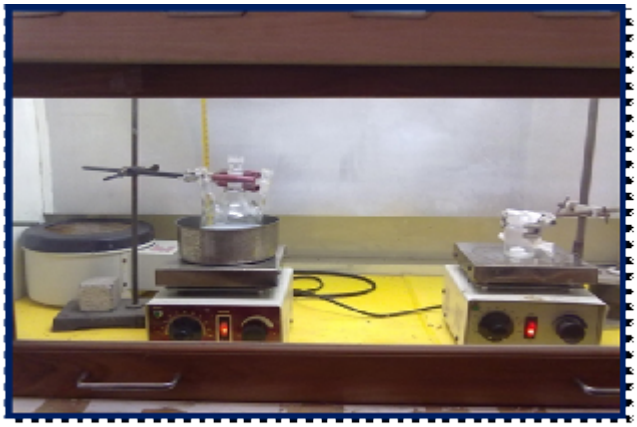

Figure 3.2: Experimental set up for the sample preparation.

The flow chart of the detailed procedure is given below:

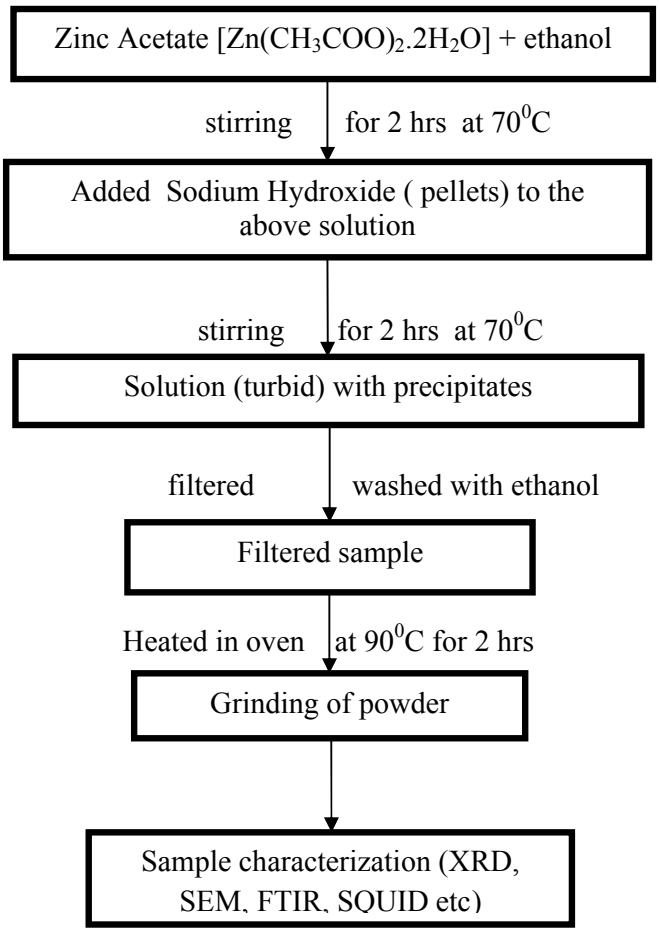

3.2.2 Synthesis of ZnO modified by transition metals (Ni,Co,Mn):

The chemicals used in this synthesis are given in the table 3.3:

Table 3.3: The list of the chemicals used for modified ZnO

Chemical name	Chemical formula	Company
Zinc acetate	$Zn(CH_3COO)_2.2H_2O$	SDFCL
Nickel acetate	$Ni(CH_3COO)_2.4H_2O$	Sigma ALDRICH
Cobalt acetate	$Co(CH_3COO)_2.4H_2O$	Lobachemie
Manganese acetate	$Mn(CH_3COO)_2.4H_2O$	Lobachemie
Ethanol	CH_3CH_2OH	SDFCL
Sodium hydroxide	NaOH	SDFCL

For different doping concentrations i.e $Zn_{1-x}M_xO$ (M=Ni, Co, Mn), the amount of materials taken are shown in the table 3.4:

Table 3.4: The Amount of the materials used for different dopant concentration

Dopant concentration X (at %)	Amount of materials taken					
	Zinc acetate (g)	Nickel acetate (g)	Cobalt acetate (g)	Manganese acetate (g)	Sodium Hydroxide (g)	Ethanol (ml)
0.25	2.197	0.006221	0.006227	0.006127	1.6	200
0.5	2.197	0.012448	0.012454	0.012254	1.6	200
1	2.197	0.024886	0.024908	0.024509	1.6	200
2	2.197	0.049772	0.049816	0.049018	1.6	200
5	2.197	0.12443	0.124541	0.122545	1.6	200

The Procedure can be explained by the following flow chart:

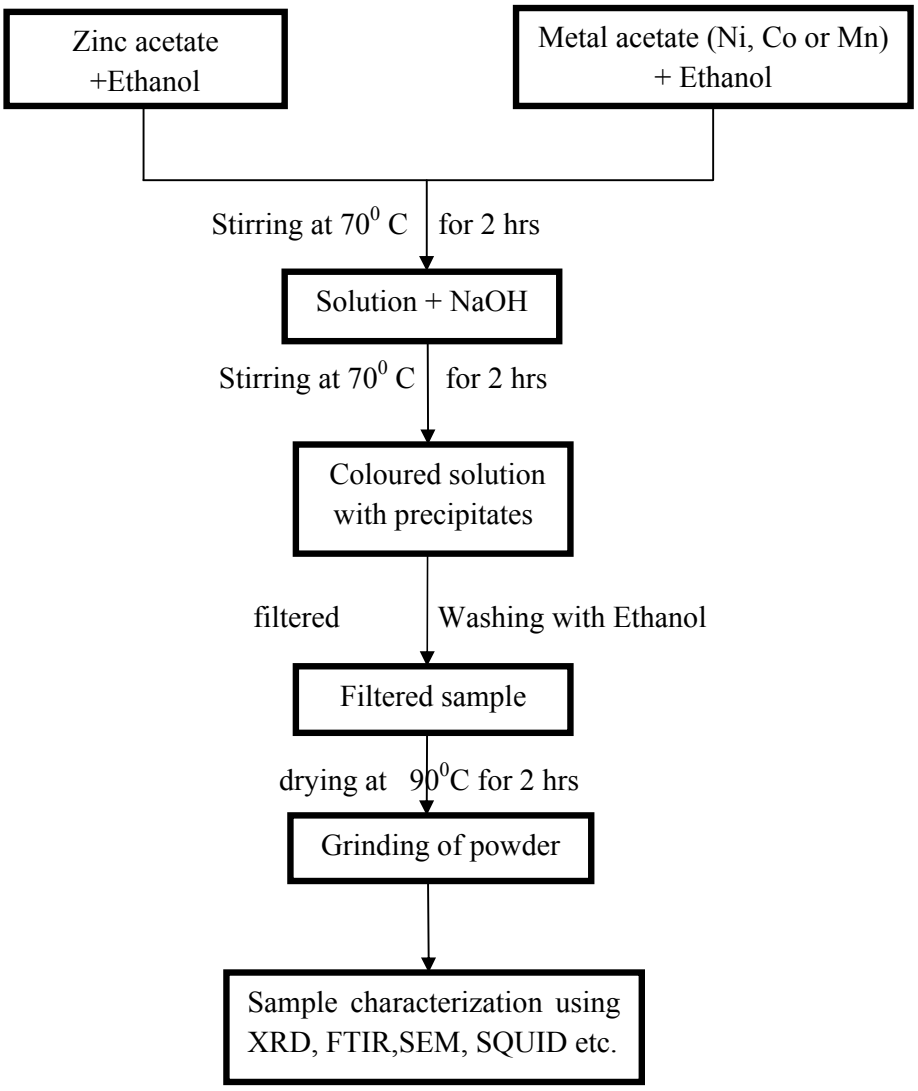

Detailed Procedure is given below:

- The glass wares (three neck round bottom flask, measuring cylinder, beaker) were cleaned and rinsed with distilled water and acetone and then dried in vacuum oven over night.
- 2.197g zinc acetate and 100 ml ethanol were charged in round bottom flask and the solution was stirred gently for 2 hours at around 70^{0}C on hot plate. Simultaneously,

metal acetate in required amount and 100 ml etahnol were taken in a beaker and stirred under same conditions.

- After two hours, both the solutions were mixed and sodium hydroxide pellets were added to the solution to adjust pH~ 10.82. Further the reaction mixture was stirred for 2 hrs at 70^0C.After that solution was allowed to cool to room temperature.
- The final product was washed with ethanol many times to make it free from the complex.
- After filtration, filtered sample was heated at 90^o C in oven for 2 hours. Finally sample was grinded and characterized using different techniques (XRD, FTIR, DTA,TGA,SQUID etc.)

3.2.3 Synthesis of ZnO modified by dopant as well as codopant:

In order to achieve the third objective, transition metal doped ZnO has been further modified by using a codopant. We made an attmpt to study the effect of codoping of Antimony on Co-doped as well as Mn-doped ZnO.

The chemicals used in this synthesis are given in the table 3.5:

Table 3.5: The list of chemicals used for codoping of ZnO

Chemical name	Chemical formula	Company
Zinc acetate	$Zn(CH_3COO)_2.2H_2O$	SDFCL
Cobalt acetate	$Co(CH_3COO)_2.4H_2O$	Lobachemie
Manganese acetate	$Mn(CH_3COO)_2.4H_2O$	Lobachemie
Antimony Chloride	$SbCl_3$	Lobachemie
Ethanol	CH_3CH_2OH	SDFCL

The amount of the different materials taken are displayed in the table 3.6 and 3.7.

1) **ZnO doped with 5% cobalt and 3% antimony:**

Table 3.6: The amount of different materials used

Zinc acetate (g)	Cobalt acetate (g)	Antimony Chloride (g)	Sodium Hydroxide (g)	Ethanol (ml)
2.197	0.12451	0.068433	1.6	200

2) ZnO doped with 5% Mn and 3% antimony:

Table 3.7: The amount of different materials used

Zinc acetate (g)	Manganese acetate (g)	Antimony Chloride (g)	Sodium Hydroxide (g)	Ethanol (ml)
2.197	0.12251	0.068433	1.6	200

The steps involed in the process are given below:

- The glass wares (three neck round bottom flask, measuring cylinder, beaker) were cleaned and rinsed with distilled water and acetone and then dried in vacuum oven.
- 2.197g zinc acetate and 100 ml ethanol were charged in round bottom flask and the solution was stirred gently for 2 hours at 70^0C on hot plate. Simultaneously, required amount of metal acetate dissolved in 50 ml Etahnol was stirred under same conditions. In another beaker, antimony chloride in required amount was dissolved in 50 ml ethanol and stirred for 2 hours at 70^0C.
- After two hours, all the three solutions were mixed and Sodium Hydroxide pellets were added to adjust pH~ 10.82. The reaction mixture was again stirred for 2 hours at 70^0C. After that solution was allowed to cool to room temperature.
- The final product was washed with ethanol many times to make it free from the complex.
- After filtration, filtered sample was heated at 90^o C in oven for 2 hours. Finally sample was grinded and characterized using different techniques (XRD, FTIR, DTA, TGA, SQUID etc.)

The procedure is summarized in the flow Chart as given below:

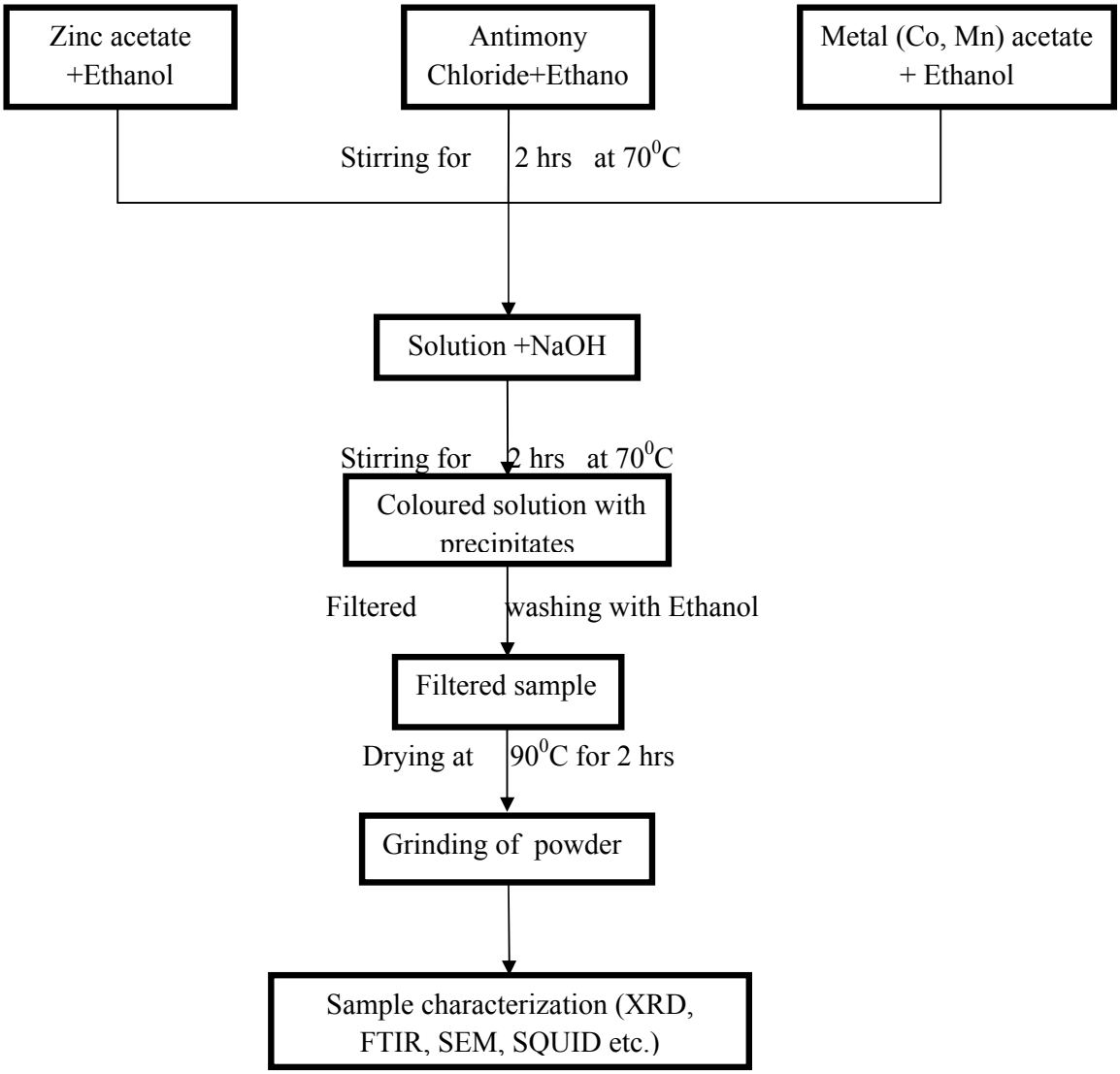

3.3 CHARACTERIZATION TECHNIQUES

3.3.1 X-Ray Diffraction Method

X-ray crystallography is a method of determining the arrangement of atoms within a crystal, in which a beam of X-rays strikes a crystal and diffracts into many specific directions. From the angles and intensities of these diffracted beams, a crystallographer can produce a three-dimensional picture of the density of electrons within the crystal. From this electron density, the mean positions of the atoms in the crystal can be determined, as well as their chemical bonds, their disorder and various other information.

In an X-ray diffraction measurement, a crystal is mounted on a goniometer and gradually rotated while being bombarded with X-rays, producing a diffraction pattern of regularly spaced spots known as *reflections* as shown in fig (4.2*)*. Crystals are regular arrays of atoms, and X-rays can be considered waves of electromagnetic radiation. Atoms scatter X-ray waves, primarily through the atoms' electrons. Just as an ocean wave striking a lighthouse produces secondary circular waves emanating from the lighthouse, so an X-ray striking an electron produces secondary spherical waves emanating from the electron. This phenomenon is known as elastic scattering, and the electron (or lighthouse) is known as the *scatterer* as shown in fig (4.1). A regular array of scatterers produces a regular array of spherical waves. Although these waves cancel one another out in most directions through destructive interference, they add constructively in a few specific directions, determined by Bragg's law:

$$2d\sin\theta = n\lambda$$

Where d is the interplanar spacing

n is the order of reflections

θ is the Bragg's angle

λ is the wavelength of X-ray used($1.54060A^0$)

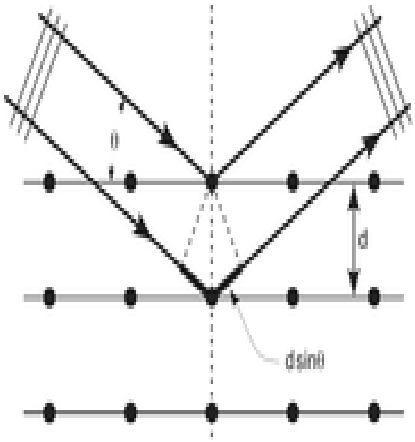

Figure 3.3: X- ray diffraction

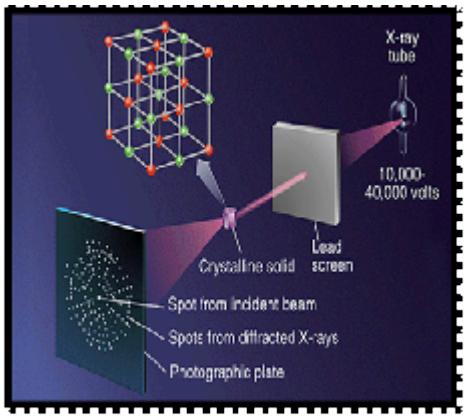

Figure 3.4: X- ray diffraction pattern

For the first order diffraction, n=1, and knowing the values of λ and θ, one can calculate the interplanar spacing d-value for a particular plane. After recording the X-ray diffraction pattern, first step involves the indexing of XRD peaks. The indexing means assigning the correct miller indexing to each peak of the diffraction pattern. The correct indexing is done only when all the peaks in the diffraction pattern are accounted for the process. There are three main methods for indexing a diffraction pattern

a) Comparing the measured XRD pattern with standard (JCPDS-cards)
b) Analytical methods
c) Graphical methods

In the case of fine particles, with the reduction in the size of the particles, the XRD lines get broadened, which indicates clearly that particle size has reduced. The line broadening can be a measure of the average size of the crystallites by using the Scherer equation:

$$\mathbf{D_v = (K\lambda) / b \cos(\theta)}$$

Where D_v is the average particle size,

K is the scherer costant,

λ is the wavelength and b is the integral breadth of the peak located located at the angle θ

Strengths and Limitations of X-ray Powder Diffraction (XRD)

Strengths

- Powerful and rapid technique for identification of an unknown minerals
- In most cases, it provides an unambiguous mineral determination
- Minimal sample preparation is required
- XRD units are widely available
- Data interpretation is relatively straight forward

Limitations

- Homogeneous and single phase material is best for identification of an unknown.
- Requires tenths of a gram of material which must be ground into a powder
- For mixed materials, detection limit is ~ 2% of sample
- For unit cell determinations, indexing of patterns for non-isometric crystal systems is complicated
- Peak overlay may occur and worsens for high angle 'reflections'

3.3.2 Fourier Transform Infrared Spectroscopy:

FT-IR stands for Fourier Transform Infrared, the preferred method of infrared spectroscopy. In infrared spectroscopy, IR radiation is passed through a sample. Some of the infrared radiation is absorbed by the sample and some of it is passed through (transmitted). The resulting spectrum represents the molecular absorption and transmission, gives information of type of bonding in the sample. This makes infrared spectroscopy useful for several types of analysis.

- FTIR can identify unknown materials
- FTIR can determine the quality or consistency of a sample
- FTIR can determine the amount of components in a mixture

The original infrared instruments were of the dispersive type. These instruments separated the individual frequencies of energy emitted from the infrared source. This was accomplished by the use of a prism or grating. A grating is a more modern dispersive element which better separates the frequencies of infrared energy. The detector measures

the amount of energy at each frequency which has passed through the sample. This results in a spectrum which is a plot of intensity Vs. frequency.

Figure 3.5 :Fourier Transform Infrared Spectrometer

Fourier Transform Infrared (FT-IR) spectrometry was developed in order to overcome the limitations encountered with dispersive instruments. The main difficulty was the slow scanning process. A method for measuring all of the infrared frequencies simultaneously, rather than individually, was needed. A solution was developed which employed a very simple optical device called an interferometer. The interferometer produces a unique type of signal which has all of the infrared frequencies "encoded" into it. The signal can be measured very quickly, usually on the order of one second. Thus the time element per sample is reduced to a matter of a few seconds rather than several minutes.

3.3.3 UV-Visible Spectroscopy

Ultraviolet-visible spectroscopy or ultraviolet-visible spectrophotometry (UV-Vis or UV/Vis) refers to absorption spectroscopy in the ultraviolet-visible spectral region (uv = 200-400 nm, visible = 400-800 nm) . In this wavelength range the absorption of the electromagnetic radiation is caused by the excitation (i.e. transition to a higher energy level) of the bonding and non-bonding electrons of the ions or molecules. A graph of absorbance against wavelength gives the sample's absorption spectrum. The measured spectrum is continuous, due to the fact that the different vibration and rotation states of the molecules make the absorption band wider.

Spectrophotometry is used for both qualitative and quantitative investigations of samples. The wavelength at the maximum of the absorption band will give information about the

structure of the molecule or ion and the extent of the absorption is proportional with the amount of the species absorbing the light. Quantitative measurements are based on Beer's Law (also known as "Lambert- Beer Law" or even "Bouguer-Lambert-Beer Law") which is described as follows:

$$A = -\log_{10}(I/I_0) = \epsilon \cdot c \cdot L,$$

where A is the measured absorbance, I_0 is the intensity of the incident light at a given wavelength, I is the transmitted intensity, L the path length through the sample, and c the concentration of the absorbing species. For each species and wavelength, ε is a constant known as the molar absorptivity or extinction coefficient. This constant is a fundamental molecular property in a given solvent, at a particular temperature and pressure, and has units of $1 / M * cm$ or often $AU / M * cm$.

The instrument used in ultraviolet-visible spectroscopy is called a UV/Vis **spectrophotometer**. It measures the intensity of light passing through a sample (I), and compares it to the intensity of light before it passes through the sample (I_o). The ratio I / I_o is called the *transmittance*, and is usually expressed as a percentage (%T). The absorbance, A, is based on the transmittance:

$$\mathbf{A = -\log(\%T / 100\%)}$$

The basic parts of a spectrophotometer are a light source, a holder for the sample, a diffraction grating or monochromator to separate the different wavelengths of light, and a detector. The radiation source is often a Tungsten filament (300-2500 nm), a deuterium arc lamp, which is continuous over the ultraviolet region (190-400 nm)— or more recently, light emitting diodes (LED) and Xenon arc lamps for the visible wavelengths. The detector is typically a photodiode or a CCD. Photodiodes are used with monochromators, which filter the light so that only light of a single wavelength reaches the detector. Diffraction gratings are used with CCDs, which collects light of different wavelengths on different pixels

A spectrophotometer can be either *single beam* or *double beam*. In a single beam instrument, all of the light passes through the sample cell. I_o must be measured by removing the sample. This was the earliest design, but is still in common use in both teaching and industrial labs.

In a double-beam instrument, the light is split into two beams before it reaches the sample. One beam is used as the reference; the other beam passes through the sample. The reference beam intensity is taken as 100% Transmission (or 0 Absorbance), and the measurement displayed is the ratio of the two beam intensities. Some double-beam instruments have two detectors (photodiodes), and the sample and reference beam are measured at the same time. In other instruments, the two beams pass through a beam chopper, which blocks one beam at a time. The detector alternates between measuring the sample beam and the reference beam in synchronism with the chopper. There may also be one or more dark intervals in the chopper cycle. In this case the measured beam intensities may be corrected by subtracting the intensity measured in the dark interval before the ratio is taken.

Samples for UV/Vis spectrophotometry are most often liquids, although the absorbance of gases and even of solids can also be measured. Samples are typically placed in a transparent cell, known as a cuvette. Cuvettes are typically rectangular in shape, commonly with an internal width of 1 cm. (This width becomes the path length, *L*, in the Beer-Lambert law.) Test tubes can also be used as cuvettes in some instruments. The type of sample container used must allow radiation to pass over the spectral region of interest. The most widely applicable cuvettes are made of high quality fused silica or quartz glass because these are transparent throughout the UV, visible and near infrared regions. Glass and plastic cuvettes are also common, although glass and most plastics absorb in the UV, which limits their usefulness to visible wavelengths.

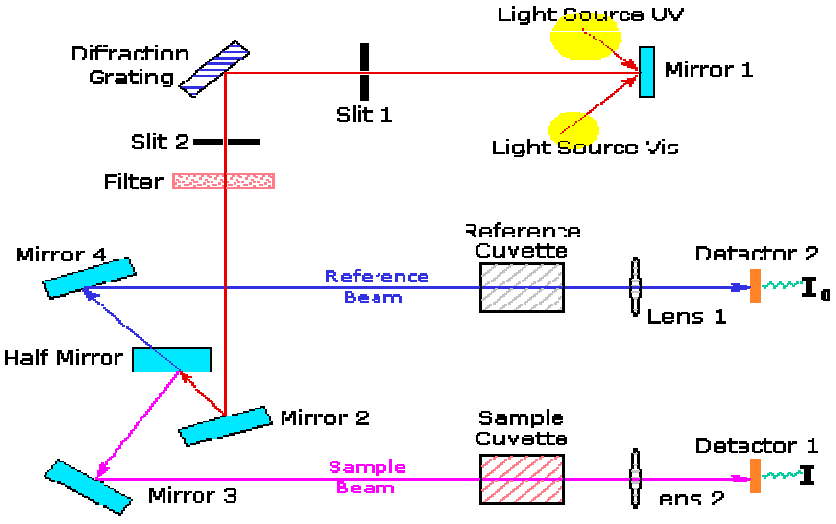

Figure 3.6 : Components of UV-Spectrophotometer

3.3.4 Differential Thermal Analysis/ Thermo Gravimetric Analysis:

An analytical method in which the specimen polymer and an inert reference material are heated concurrently at a linear rate, each having its own temperature sensing and recording apparatus. The thermal-energy changes, either endothermic or exothermic, which occur in the course of heating, are plotted. This thermogram provides data on the chemical and physical transformations that have occurred, such as melting, sublimation, glass transitions, crystal transitions, and crystallization.

A DTA consists of a sample holder comprising thermocouples, sample containers and a ceramic or metallic block; a furnace; a temperature programmer; and a recording system. The key feature is the existence of two thermocouples connected to a voltmeter. One thermocouple is placed in an inert material such as Al_2O_3, while the other is placed in a sample of the material under study. As the temperature is increased, there will be a brief deflection of the voltmeter if the sample is undergoing a phase transition. This occurs because the input of heat will raise the temperature of the inert substance, but be incorporated as latent heat in the material changing phase. Fig (3.9) shows a DTA/TGA apparatus.

Figure 3.7: DTA/TGA

A DTA curve can be used only as a *finger print* for identification purposes but usually the applications of this method are the determination of phase diagrams, heat change measurements and decomposition in various atmospheres.

Thermo gravimetric Analysis (TGA) is a type of testing that is performed on samples to determine changes in weight in relation to change in temerature. Such analysis relies on a high degree of precision in three measurements: weight, temperature, and temperature change. As many weight loss curves look similar, the weight loss curve may require transformation before results may be interpreted. A derivative weight loss curve can be used to tell the point at which weight loss is most apparent. TGA is commonly employed in research and testing to determine characteristics of materials such as polymers, to determine degradation temperatures, absorbed moisture content of materials, the level of inorganic and organic components in materials, decomposition points of explosives, and solvent residues.

It is also often used to estimate the corrosion kinetics in high temperature oxidation. The analyzer usually consists of a high-precision balance with a pan (generally platinum) loaded with the sample. The pan is placed in a small electrically heated oven with a thermocouple to accurately measure the temperature. The atmosphere may be purged with an inert gas to prevent oxidation or other undesired reactions. A computer is used to control the instrument. Analysis is carried out by raising the temperature gradually and plotting weight against temperature. The temperature in many testing methods routinely reaches 1000°C or greater, but the oven is so greatly insulated that an operator would not be aware of any change in temperature even if standing directly in front of the device. After the data is obtained, curve smoothing and other operations may be done such as to find the exact points of inflection. A method known as hi-res TGA is often employed to obtain greater accuracy in areas where the derivative curve peaks. In this method, temperature increase slows as weight loss increases. This is done so that the exact temperature at which a peak occurs can be more accurately identified.

3.3.5 Scanning Electron Microscopy :

Scanning electron microscopy (SEM) is basically a type of electron microscope. SEM is used for various purposes;

- Topographic studies.
- Microstructure analysis.
- Elemental analysis if equipped with appropriate detector (energy/wavelength dispersive x-rays).
- Chemical composition.
- Elemental mapping.

In SEM, Primary electrons are thermonically or field emitted by a cathode filament (W or LaB)) or a filed emission gun (W-tip) and after that accelerated with high energy typically 1-30KeV. The electron beam is steered with scanning coils over the area of the interest. Upon interaction with material, the primary electrons decelerate as well as losing their energy, transfer it inelastically to other atomic electron and to the lattice. Due to continuous scattering events the primary beam spread up with different energies depending on source origin.

Secondary electrons (1-50eV) are mostly used for the imaging the topographically contrast and reproduce the surface. High energy elastically backscattered electrons depends on the atomic number (Z) of the element, which is useful to obtain Z-constrat. X-ray characteristics can be used to qualitatively and quantitatively analyze the elemental composition and distribution in the sample.

Figure 3.8: Scanning Electron Microscope

3.3.6 Magnetic characterization using SQUID

The superconducting quantum interference device (SQUID) is a Josephson junction which consists of a split superconducting ring that contains a thin insulating gap. The two superconductor sections separated by a thin insulating layer can experience tunneling of Cooper pairs of electrons through the junction. There are two types of SQUIDs: a) Alternating current (AC or RF) having one Josephson junction and b) Direct current (DC) having two Josephson junctions. The DC SQUID is more sensitive than the AC squid. The principle of the DC SQUID is that the wavefunctions for the Cooper pairs of electron

tunneling across the two Josephson junctions in the DC SQUID can undergo quantum mechanical interference that depends on the applied magnetic field present in the loop. If a constant biasing current is maintained in the SQUID device, the measured voltage oscillates with the changes in phase at the two junctions and depends upon the change in the magnetic flux. Thus, by counting the oscillations one can measure the flux change that has occurred. The minimum magnetic field that can be measured using a SQUID is of the order of 10^{-14} Tesla. Figure 4.9 shows a schematic of a Josephson junction used in a SQUID magnetometer

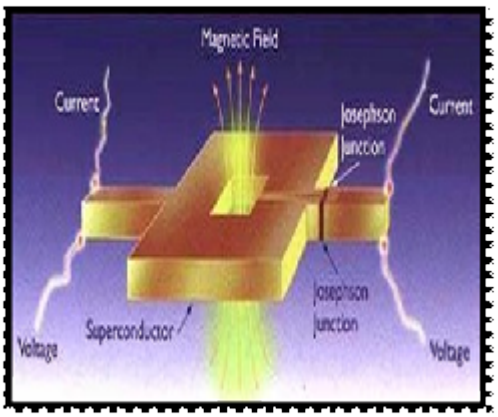

Figure 4.9: A schematic of a Josephson Junction in a SQUID

Figure 4.10: Exernal view of SQUID

The magnetic properties that can be measured using SQUID magnetometer are :-

1. Magnetization vs Applied field (Hysteresis) :- Here a magnetic field is applied and swept from zero up to a positive value such that saturation magnetization is reached and then back through zero to a negative value and then back to the positive value through zero field. The parameters obtained from hysteresis measurement are coercivity (Hc), saturation magnetization (Ms) and saturating field (Hs).
2. Field cool(FC) Magnetization vs Temperature measurements : Here, the sample is cooled from 300 K under an applied field (FC) to 5K and then heated back to 300 K under the same applied field. During the heating cycle the magnetization is measured as a function of time. This technique provides information of any transition in magnetic behaviour like the Curie temperature (Tc).
3. Zero field cool Magnetization vs Temperature measurements : Here, the sample is first heated above the magnetic blocking temperature and then cooled down to a low temperature(~5K) without applying any field. Then at 5 K a field is applied and the

sample is heated under the applied field to 300 K and magnetization is measured as a function of time. The FC and the ZFC curves will depart at the blocking temperature if some precipitate or nanoclusters are present. This departure is a signature of both a secondary phase and a superparamagnetic phase. Measurements of magnetoresistance (MR) on the various DMS samples can done by using a Quantum Design physical property measurement system (PPMS) equipped with a SQUID coil. The magneto resistance can also be measured using a four point probe configuration in the presence of an applied magnetic field.

Chapter-4

Results and Discussions

This chapter summarized the results obtained from X-Ray Diffraction technique (XRD), Fourier Transform Infrared Spectroscopy (FTIR), UV-Visible Spectroscopy, Scanning Electron Microscopy and Magnetic measurements (SQUID).

4.1 Structural Analysis :

4.1.1 XRD analysis for pure ZnO:

The crystal structure of synthesized samples have been investigated using X-Ray Diffractometer (Philips X'Pert Pro). The X-ray diffraction patterns of various samples of ZnO have been recorded using CuK_α radiations (λ=1.54060 A^0) in the range of 2θ - 5 to 65^0 C Figure 5.1 shows the diffractrogram obtained for commercially avaible ZnO and for the synthesized one.

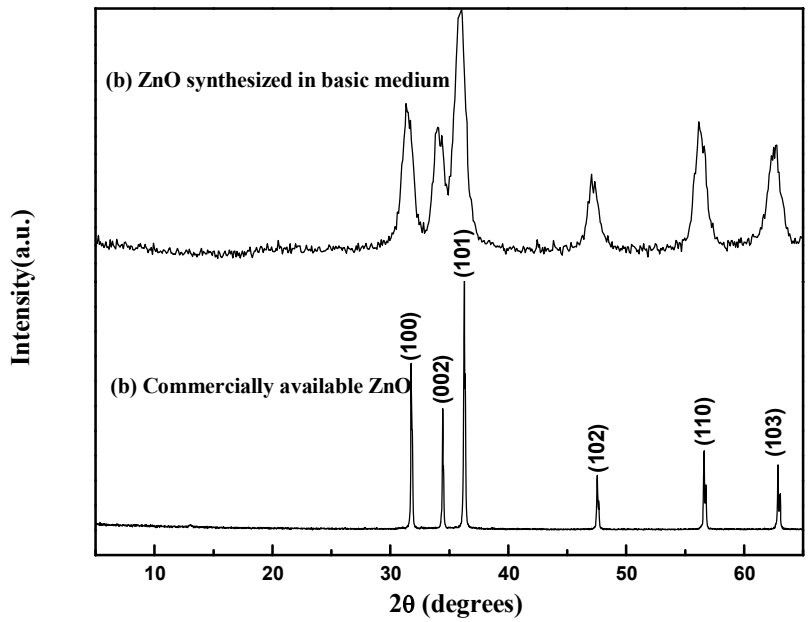

Figure 4.1:X-ray diffractogram of (a) Commercially available ZnO and (b) Synthesized ZnO

We found that highly intense peaks with good broadening were observed in the diffractogram indicating the crystalline nature of the sample. The peaks observed at the positions 2θ =31.5^0, 33.9^0, 35.9^0, 47.2^0, 56.2^0 and 62.3^0 corresponds to the lattice planes (100) ,(002), (101), (102),(110),(103) respectively, indicative of Wurtzite hexagonal

crystal structure of ZnO. All the peaks are matched with standard JCPDS card no. 50664. Also the broadening of the peaks in case of synthesized sample as compared to that of commercially available, infer about the decrease in particle size.

The average particle size of the sample has been calculated using Debye Scherrer formula:

$$D=0.9\,\lambda\,/\{\sqrt{(B_0^2-B_a^2)}\,\cos\theta\}\ldots\ldots\ldots\ldots\ldots\ldots\ldots\ldots(4.1)$$

Where D is the average particle size

λ is the wave of the radiations used(1.54060A^0)

B_0 is the full width at half maximum of the diffraction peak for the synthesized ZnO

B_a is the full width at half maximum of the diffraction peak for the commercially available ZnO

θ is the angle corresponding to that peak

For the above diffractogram, the calculated average particle size is about **7-26 nm.**

The lattice constants for both samples have been calculated using the formula:

$$\frac{1}{d^2}=\frac{4}{3}\left(\frac{h^2+k^2+hk}{a^2}\right)+\frac{l^2}{c^2}\qquad\ldots\ldots\ldots\ldots\ldots\ldots\ldots\ldots\ldots\ldots\ldots\ldots(4.2)$$

Where d is the inter planar spacing

h, k, l are the miller indices for the plane

a and **c** are lattice parameters

The lattice constants calculated have been shown in the table below 4.1:

Table 4.1: lattice constants for commercially available and synthesized pure ZnO

Sample name	Lattice constants		c/a
	a(A^0)	c(A^0)	
Commercially available ZnO	3.252179	5.2152	1.6036
Synthesized ZnO	3.27543	5.28442	1.6133

4.1.2 XRD analysis for Ni doped ZnO:

Figure 4.2 shows the X-ray diffraction patterns for Nickel doped ZnO. It has been observed that the sample continues to retain the wurtzite hcp structure with the increase in Ni content upto 5%.which reveals that all the Ni atoms properly fit in the valence site of Zn without disturbing the structure. The absence of any extra peak also confirms the successful doping.

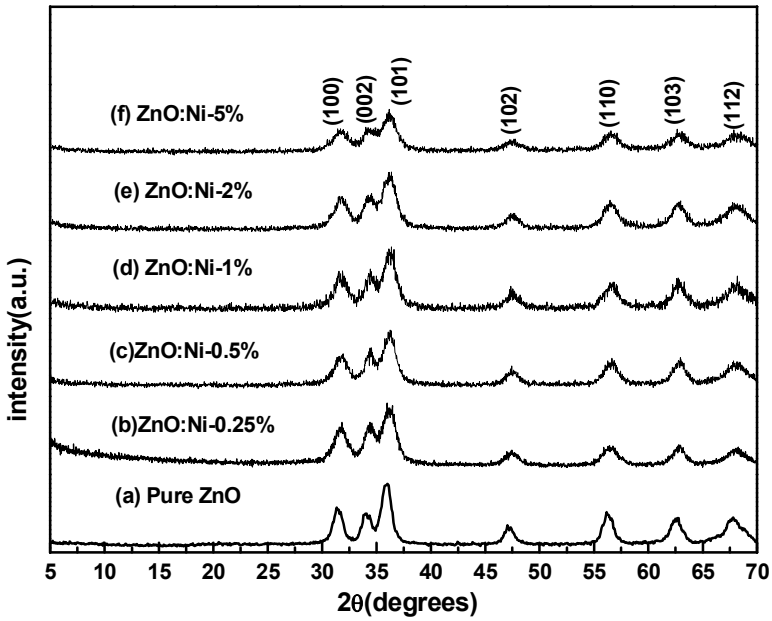

Figure 4.2: XRD pattern for pure ZnO and Ni doped ZnO

The average particle size and lattice constants of all the samples have been calculated using the equation (4.1) and (4.2) respectively. The calculated average particle size and lattice constants for pure and Ni-doped samples are given in the table 4.2 below.

Table 4.2: Average particle size and lattice constants for pure and Ni-doped ZnO

Nickel content (at%)	Average particle size (nm)	Lattice constants		c/a
		a(A^0)	c(A^0)	
pure ZnO	7	3.27	5.28	1.6133
0.25%	89	3.26	5.23	1.6101
0.5%	25	3.25	5.19	1.6071
1%	10	3.24	5.15	1.5964
2%	14	3.26	5.28	1.6169
5%	9	3.29	5.27	1.5988

We found that, with Doping of nickel, the average particle size has been increased first at lower concentrations and then declined to lower value at higher concentration of Ni, though the particle size remains greater than pure one in magnitude. The variation of average particle size with increase in Ni concentration is shown in the figure 4.3.

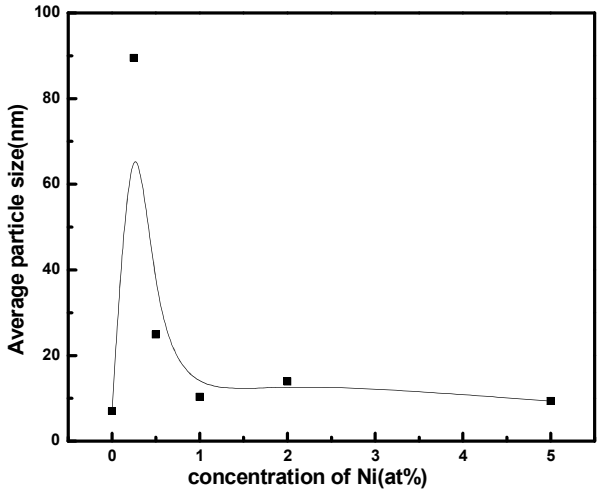

Figure 4.3: Average particle size as a function of Ni-concentration

It is clear from the table 4.2, that the lattice constants and c/a value of ZnO gets decreased in small amount with the doping of nickel. Also, With increase in nickel concentration, the lattice constants first decreases and then increases. Such behaviour has been attributed to the fact that the Zn^{2+} ions are replaced by Ni^{2+} ions having ionic radius ($0.55A^0$) slightly

less than that of Zn^{2+} ion ($0.60A^0$) in the tetrahedral coordination. Thus, the substitution of Ni^{2+} in ZnO causes the decrease in lattice parameters and hence reflects the lattice contraction. The variation of Lattice constants a and c with Ni concentration is plotted in the figure 4.4(a) and 4.4(b) respectively.

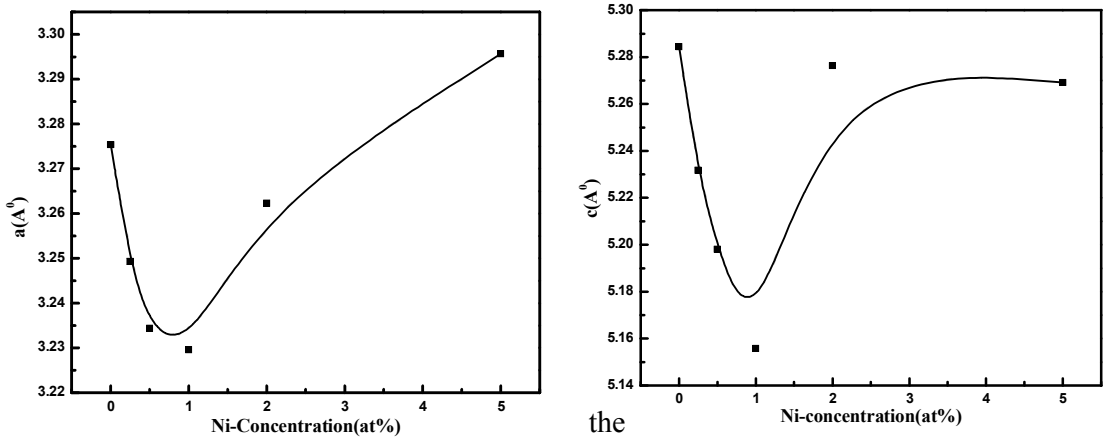

Figure 4.4: Variation of lattice constants **a** and **c** with Ni-concentration
(b)

4.1.3 XRD analysis for Co doped ZnO:

Figure 4.5 shows the X-ray diffraction pattern for the ZnO doped with different concentrations of cobalt and codoped (antimony).All the diffraction peaks have been matched with card no. 50664 indicating the formation of Wurtzite hexagonal crystal structure. For Co-doped ZnO, we obtained highly intense peaks whereas the sample having codopant seems less cryatalline as the intensity of the peaks diffused, however the diffraction signatures obtained for this sample are same as others and matched with card no. 50664. Thus it is quite reasonable to say the the crystallinity of the sample has been disturbed upto some extent with the codopant.

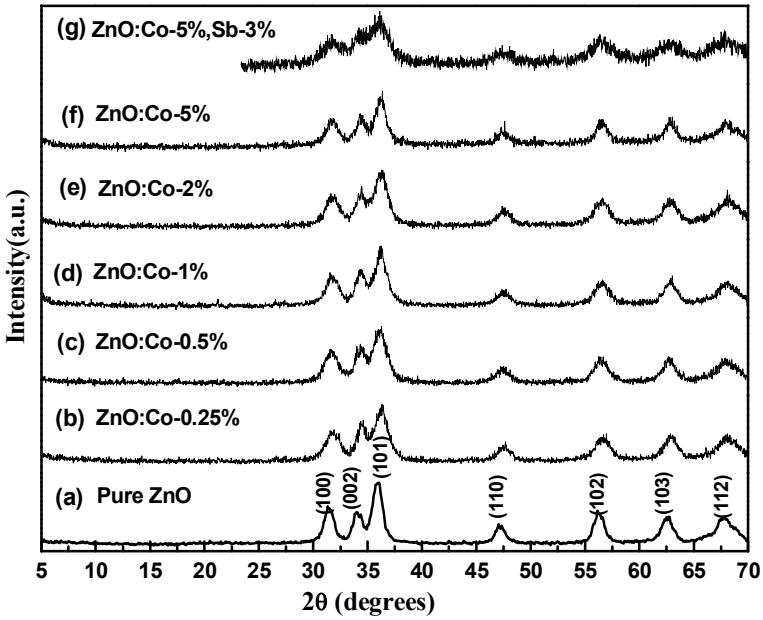

Figure 4.5: X –ray diffraction patterns for pure ,Co-doped ZnO and codoped (antimony)

The average particle size and the lattice parameters for all these samples were calculated using equation 4.1 and 4.2 and are shown in the table 4.3:

Table 4.3: Average particle size and lattice constants for pure, Co-doped ZnO and codoped (antimony)

Cobalt Content (at%)	**Average particle size (nm)**	**Lattice constants**		**c/a**
		a (A^0)	**c** (A^0)	
pure ZnO	7	3.27543	5.28442	1.6133
0.25	25	3.27563	5.20256	1.58826
0.5	9	3.25845	5.28111	1.620743
1	14	3.28063	5.2160	1.58994
2	8	3.23134	5.20608	1.61112
5	30	3.25431	5.22278	1.604881
Co-5%,Sb-3%	4.9	3.25786	5.2504	1.61161

Note that the particle size was found higher than that of pure ZnO. However it does not show any regular variation with the increase in Cobalt content as displayed in the table 5.3 and figure 4.6.

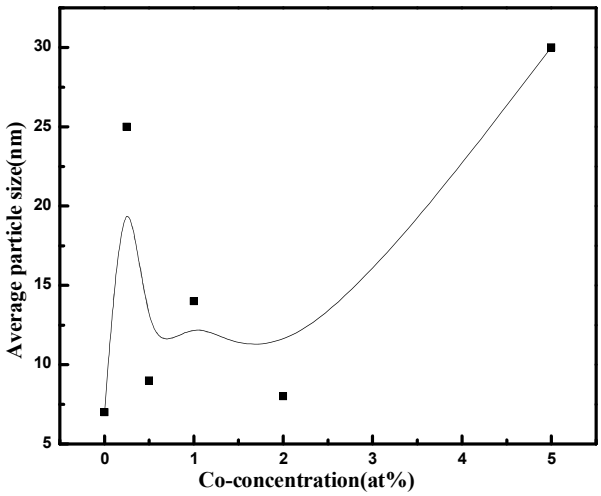

Figure 4.6: Variation of average particle size with the Co concentration

The lattice constants also does not show any regular variation with the Cobalt content as shown in figure 4.7. However in the literature, It has been reported that the lattice parameters increase with the increase in Cobalt Concentration. We are trying to finf out the exact reason for such peculiar behaviour in these sample.

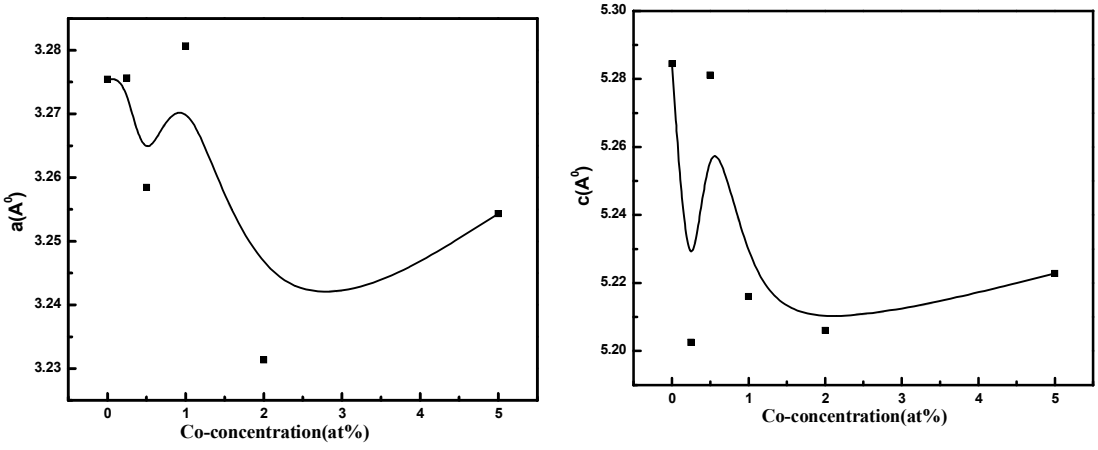

Figure 4.7: Variation of lattice constants with Co concentration

4.1.4 XRD analysis for Mn doped ZnO:

X-ray diffractograms obtained for ZnO doped with different concentrations of Manganese (Mn) ions and also with codopant (Antimony) are shown in the figure 4.8:

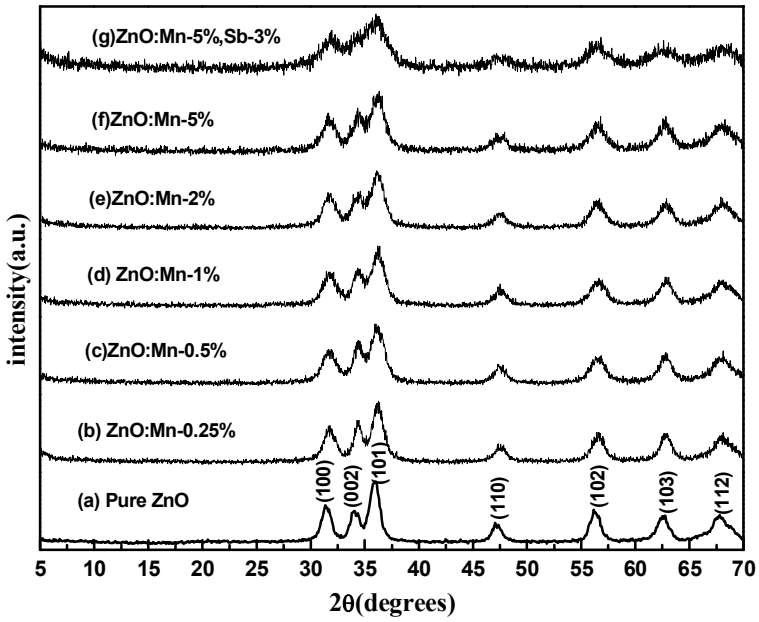

Figure 4.8: X-Ray Diffraction Pattern for Pure and Mn doped ZnO and codoped (antimony)

All the samples exhibit wurtzite hexagonal crystal structure as all the diffraction peaks match with card no. 50664 . No extra peak obtained with doping indicates that the dopant ion successfully sit in the valence site without disturbing the structure upto 5%. However with codopant, we found that the sample is less crystalline and the (002) reflection gets diffused whereas rest of the reflections corresponds to the Wurtzite Hexagonal crystal structure.

The average particle size and lattice parameters for all the samples have been calculated using equation 5.1 and 5.2 and are shown in the table 5.4:

Table 4.4: The average particle size and lattice constants for pure, Mn-doped Zno and codoped (antimony)

Manganese Content (at%)	Average particle size (nm)	Lattice constants		c/a
		a (A^0)	**c** (A^0)	
pure ZnO	7	3.27543	5.28442	1.6133
0.25	8	3.24904	5.21692	1.6057
0.5	12	3.2497	5.21	1.60358
1	30	3.26657	5.21	1.59791
2	17	3.2449	5.20	1.5971
5	14	3.27314	5.21	1.5920
Mn-5%,Sb-3%	12	3.25166	5.23	1.6089

It has been observed that the average particle size of the sample increases with Mn doping upto 1% and then declined as shown in the figure 4.9 below.

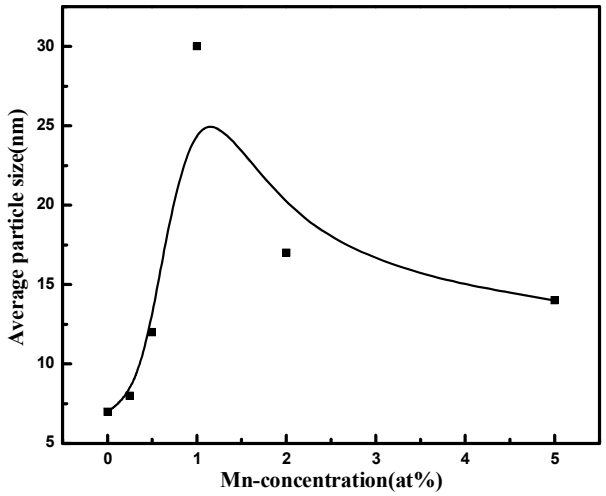

Figure 4.9: Variation of average particle size with Mn concentration

The lattice parameters for Mn-doped samples are approximately same as that of puer ZnO. and does not show any regular variation with increase in Mn content as displayed in figure 4.10. However, In literature, it has been reported that the substitution of Mn ion in ZnO

leads to an increase in the lattice parameters, Since the ionic radius of Mn^{2+} ion (0.66 A^0) is larger than that of Zn^{2+} (0.60 A^0).

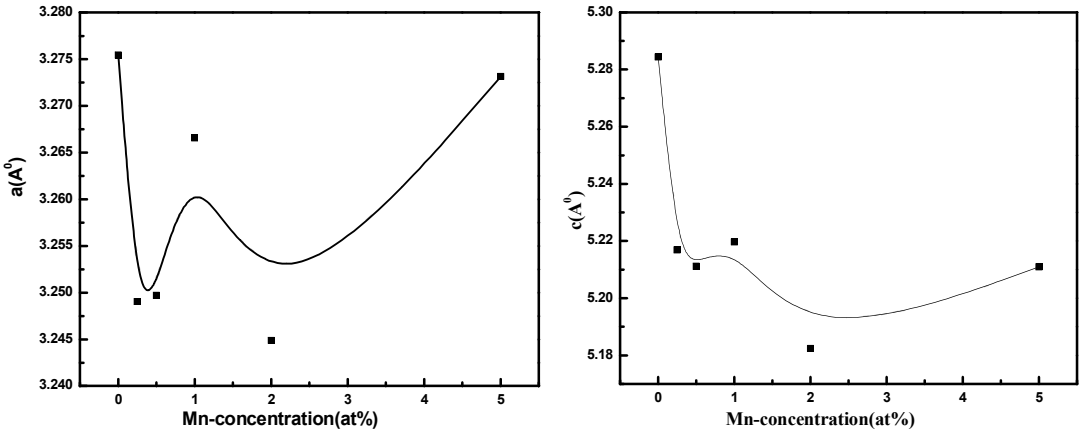

Figure 4.10: Variation of lattice parameters with Mn content

4.2 Chemical Analysis

The chemical analysis of all the synthesized samples have been done using Fourier Transform Infrared (FTIR) Spectrometer (Perkin Elmer Spectrum BX II) in the wavenumber range 400-4000 cm^{-1}

4.2.1 FTIR spectra for pure ZnO:

The FTIR spectra for pure ZnO are displayed in the figure 4.11. Different peaks obtained correspond to the different bonds present in the sample. Peaks observed at 2369.947cm^{-1} and 2341.318cm^{-1} are due to the presence of stretching and vibrations of C-H bond. Peak observed at 1540.315cm^{-1} corresponds to the COO^- group, which may be due to some residue of the precursor Zinc Acetate used in the reaction. The reflection observed at 674.700 cm^{-1}shows the presence of Cis-disubstituted alkenes.The major peak observed at 452.79cm^{-1} is the indicative signature confirming the formation of ZnO. The extra peaks observed in this sample can be removed with little heat treatment to make ZnO free from the complex.

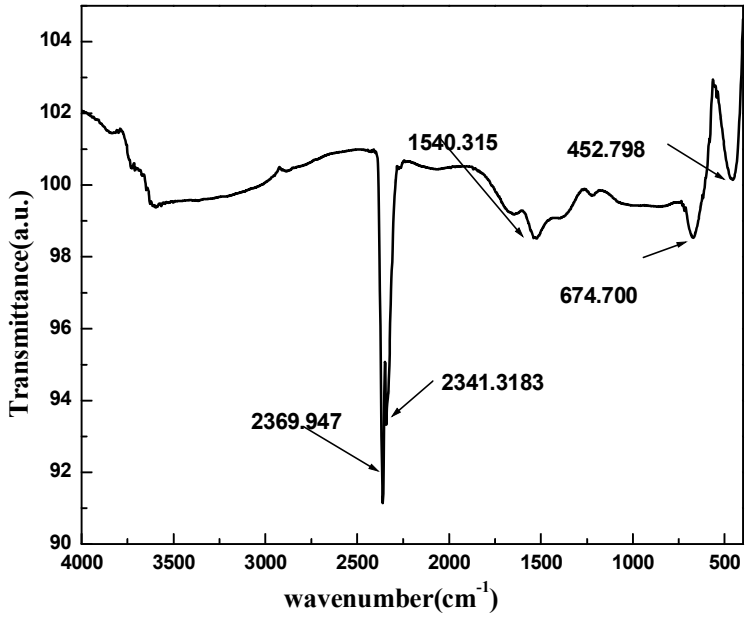

Figure 4.11: FTIR spectra of pure ZnO

4.2.2 FTIR spectra for Ni-doped ZnO

Figure 4.12 shows the FTIR spectra for pure and Ni- doped ZnO.

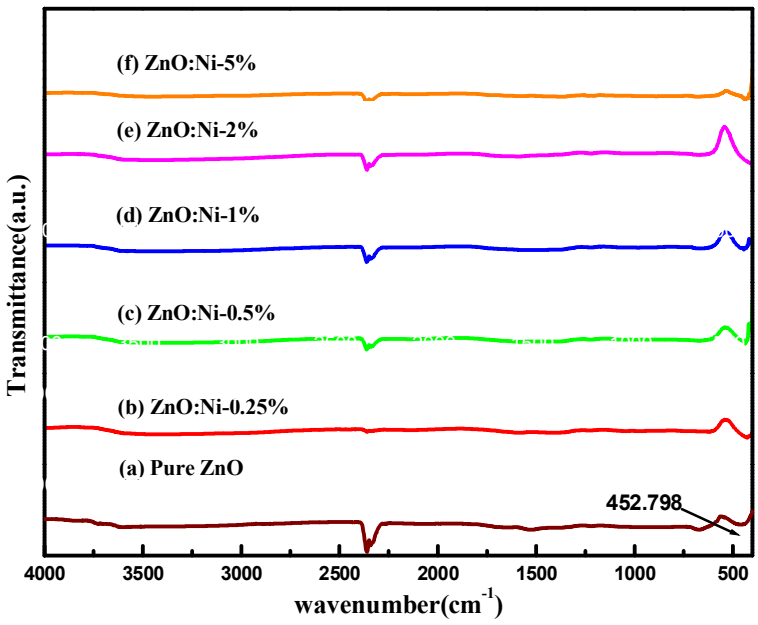

Figure 4.12: FTIR spectra for pure and Ni doped ZnO

The reflection in the region 430-460 cm^{-1} clearly reveals the formation of Zn-O bond. Also the absence of any other peak in the spectra infers that ZnO is free from the complex.

4.2.3 FTIR spectra for Co-doped ZnO:

Figure 4.13 shows FTIR spectra for pure, Co-doped and antimony codoped ZnO samples. In all the spectra, peak around 450 cm^{-1}, corresponding to Zn-O bond has been obtained and there is no extra peak corresponding to other reactants giving primary idea that Co has been substituted in place of Zn properly and not free in the complex. FTIR studies give supplementary information about ZnO formation, which is in good agreement with the information obtained from XRD.

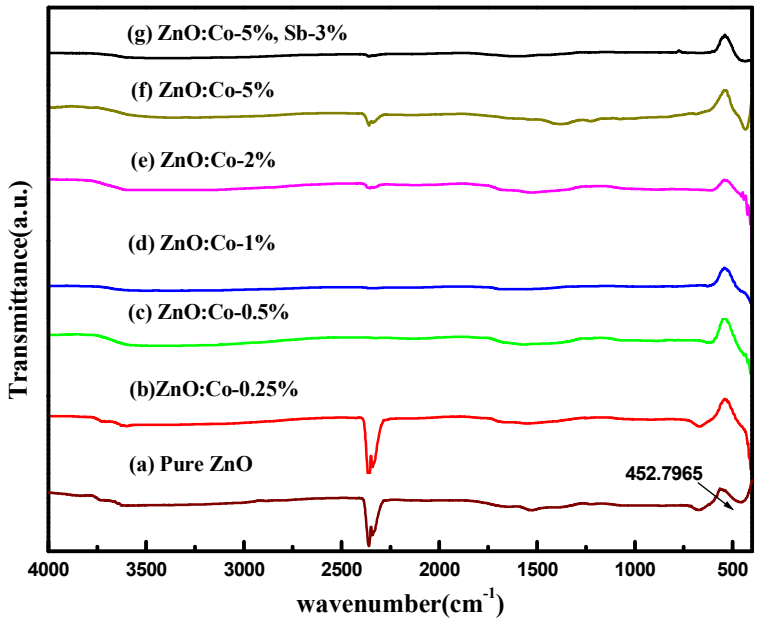

Figure 4.13: FTIR spectra for pure, Co-doped and antimony codoped ZnO

4.2.4 FTIR spectra for Mn-doped ZnO

Figure 4.14 displays the FTIR spectra for pure, Mn-doped and antimony codoped ZnO. All the spectra show peak around 450 cm^{-1} corresponding to Zn-O bond Stretching. No characteristic reflection of Mn-O bond and any other reactant seen in the spectra. The absence of any secondary peak reveals that ZnO is free from complex and dopant fit properly in the valence site of Zn.

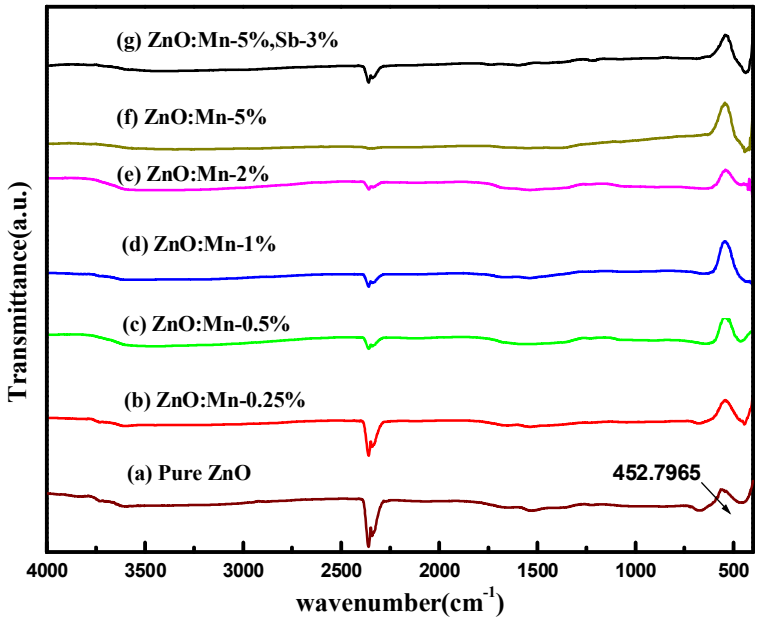

Figure 4.14: FTIR spectra for pure, Mn-doped and antimony codoped ZnO

4.3 Optical studies:

Optical measurements for all the synthesized samples have been performed using UV-Visible spectrophotometer (**lambda 25 Perkin Elmer**) in the wavelength range 250-550 nm.

4.3.1 UV-Visible Spectrum for pure ZnO

The electronic absorption spectrum of pure ZnO obtained from UV-Visible spectroscopy is shown in the figure 4.15.The exciton absorption has been observed at 362.0168 nm, which is less than that of bulk ZnO (380 nm) by 18 nm and hence infer about the blue shift. The energy band gap corresponding to the absorption wavelength has been calculated using the relation:

$$E_g = hc/\lambda \ldots\ldots\ldots\ldots\ldots\ldots\ldots\ldots\ldots (4.3)$$

Where h is Planck's constant, c is the speed of light in vacuum, λ is the absorption wavelength .

The calculated band gap of the synthesized sample is around 3.42525 eV. The increase in the band gap of the synthesized sample as compared to that of bulk ZnO (3.26 nm) reveals the reduction of the particle size upto nanoscale as also reflected in the XRD analysis

Such shift in the band-bap is attributed to the fact that at nano-level, when the particle size becomes smaller than the Bohr exciton radius, the quantum confinement occurs and the formation of discrete energy levels in valence band and conduction band leads to the increase in band gap.

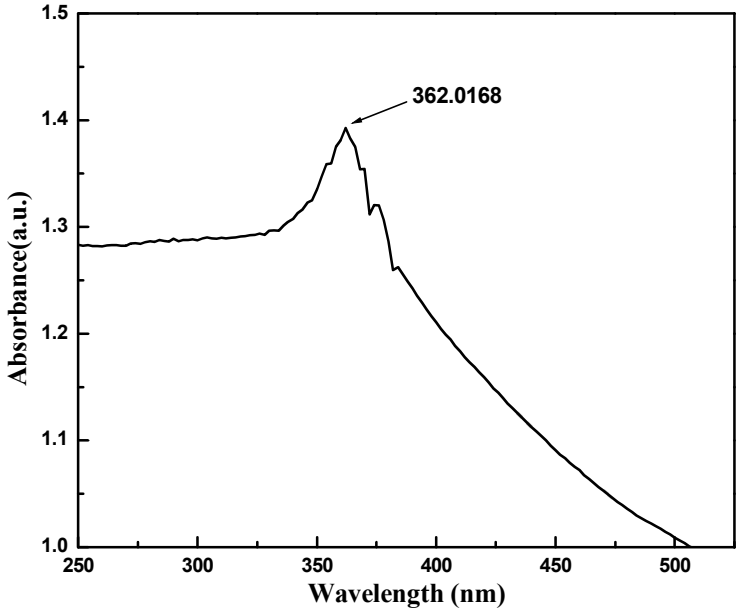

Figure 4.15: UV-Visible spectrum for pure ZnO.

4.3.2 UV-Visible Spectra for Ni-doped ZnO:

Figure 4.16 presents the UV-Visible spectra for the pure and Ni-doped ZnO. It has been observed that with the doping of nickel, the absorption wavelength shifts to the higher value than that of the synthesized pure ZnO. Hence the band gap of the material decreases . This effect has been attributed to the fact that, the doping of nickel introduces some trap levels between valence band and conduction band. The radiative transitions, which were initially occurring from band to band, now begins to take place from these trap levels and thus decrease the band gap. With further increase in nickel concentration (upto 2%), absorption wavelength shifts to higher values resulting decrease in band gap.

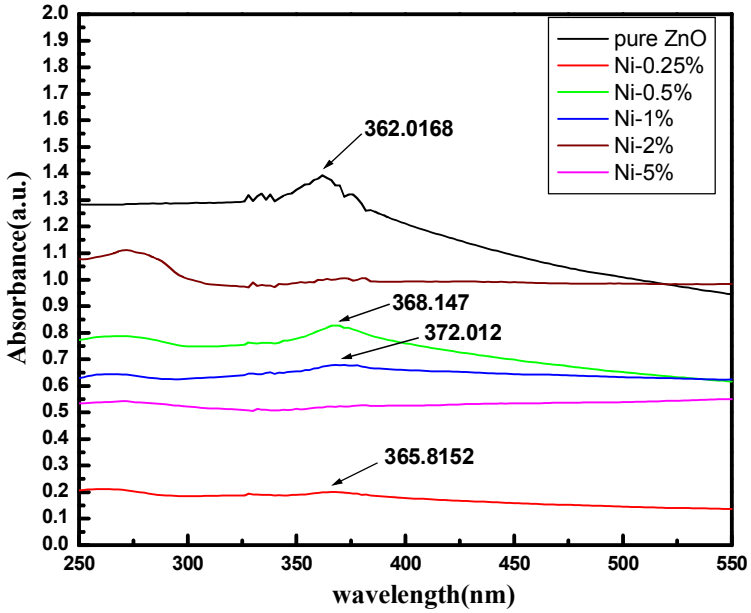

Figure 4.16: UV-Visible spectra for pure and Ni-doped ZnO

Table 4.5 summarizes the variation of absorption wavelength and band gap with nickel content and also plotted in figure 4.17

Table 4.5: Values of band gap for different Ni-concentrations

Ni content (at%)	absorption wavelength (nm)	Band gap (eV)
0	362.0168	3.425
0.25	365.8152	3.382
0.5	368.147	3.361
1	372.012	3.326
2	380.408	3.259
5	380.9521	3.255

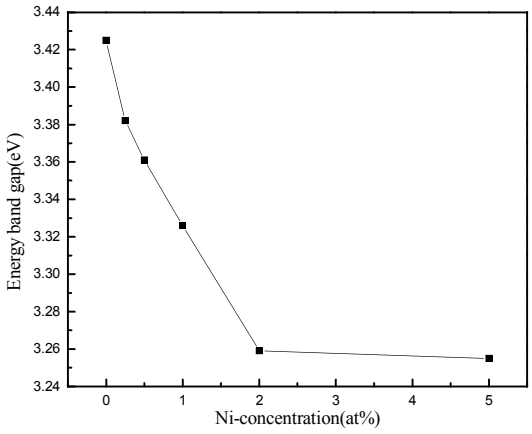

figure 4.17: Variation of band gap with Ni-concentration

4.3.3 UV-Visible spectra for Co-doped ZnO

Figure 4.18 shows UV-visible spectra carried out for pure ZnO, Co-doped and antimony codoped ZnO.

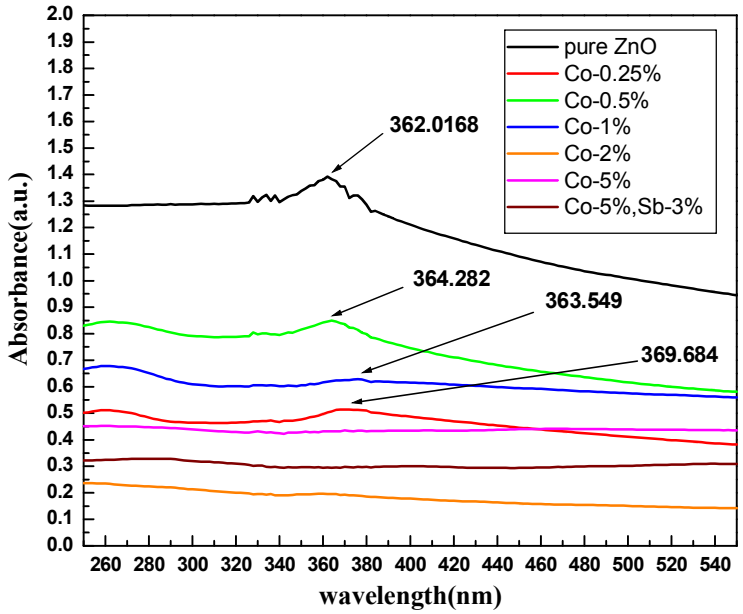

Figure 4.18: UV-Visible spectra for pure, Co-doped and antimony codoped ZnO

It has been observed that, with the cobalt doping, the absorption wavelength gets shifted to higher value following the same trend as in case of Ni. However as the system becomes cobalt rich, the wavelength shifts to lower value, resulting in increment in the band gap.

The values of absorption wavelength and band gap for different Co concentration are given in the table 4.6 and the variation is plotted in figure 4.19.

Table 4.6: Values of Band-gap at different Co-concentrations

Co content (at%)	absorption (nm)	Band gap (eV)
0	362.0168	3.425
0.25	369.680	3.347
0.5	364.282	3.397
1	363.549	3.404
2	360.417	3.440
5	356.153	3.481

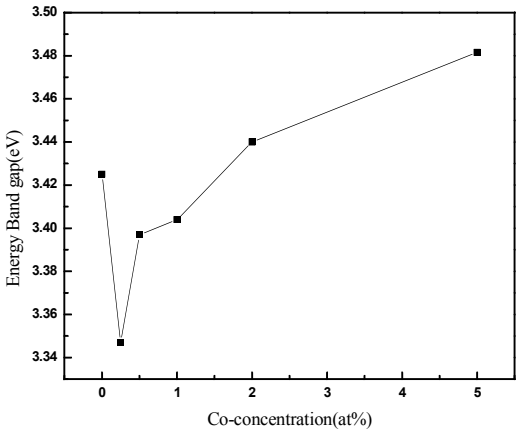

Figure 4.19: Variation of band gap with Co-concentration

4.3.4 UV-Visible spectra for Mn-doped ZnO

UV-Visible spectra carried out for Pure , Mn-doped and antimony codoped ZnO are shown in the figure 5.20. In case of Mn-doping, the wavelength shifts to the higher values resulting in the decrement in the band gap upto higher concentration.

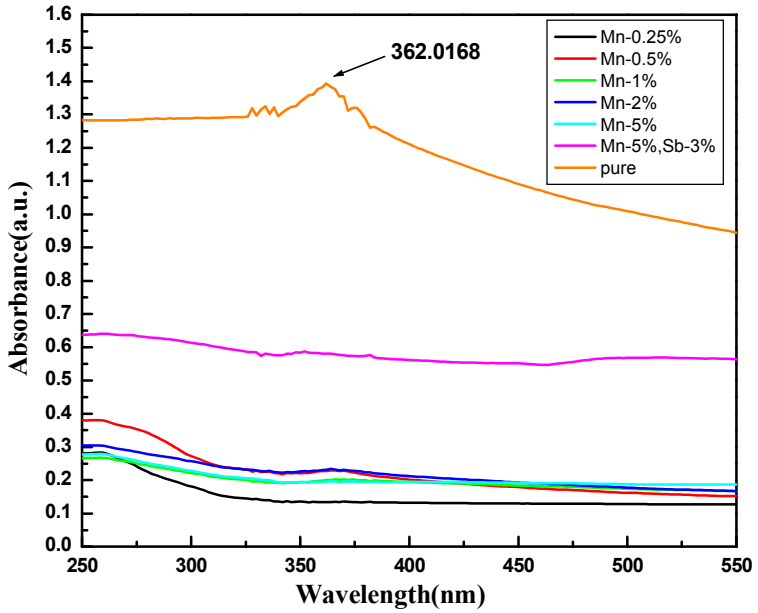

Figure 4.20: UV-Visible spectra for pure, Mn-doped and Sb codoped ZnO

For different concentration of Mn, the values of absorption wavelength and band gap are shown in the following table 4.7 and band gap Vs Mn concentration has been plotted in figure 4.21.

Table 4.7: Values of band gap at different Mn concentrations

Mn content (at%)	absorption wavelength (nm)	Band gap (eV)
0	362.0168	3.425
0.25	364.321	3.404
0.5	365.815	3.383
1	368.147	3.361
2	371.213	3.342
5	371.352	3.333

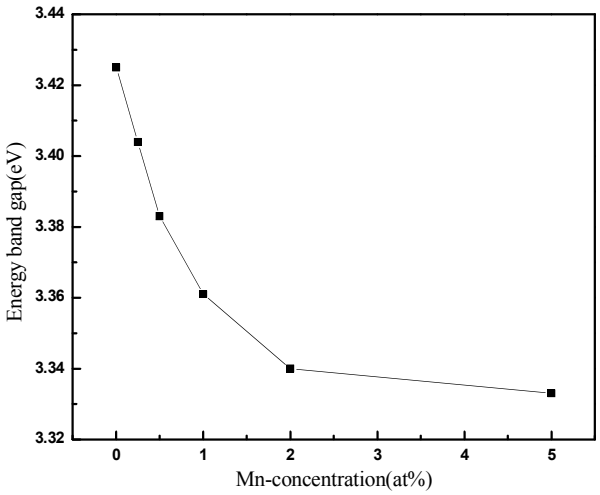

Figure 4.21: Variation of band gap with Mn concentration

From the above analysis, it can be summarized that the addition of Ni and Mn leads to the decrease in the band gap, which may be due to the formation of some trap levels between valence band and conduction band. Whereas, the doping of Co gives rise to increase in the band gap.

4.4 Thermal Analysis

Thermal analysis of the pure ZnO has been carried out using (Perkin Elmer Diamond TG/DTA) to understand the stability and thermodynamic change in the synthesized samples at higher temperature.

4.4.1 Thermogravimetric Analysis of pure ZnO:

Figure 4.22 shows the variation in wt% loss with temperature. The small peak obtained at 150^0C corresponds to the evaporation of moisture from the sample. The weight loss from 150^0C to 400^0C is mainly due to removal of the carbonaceous compounds and lower melting additives from the sample. At higher temperature, there is a negligible weight loss in the sample, which clearly indicates the stability of phase. Second weight loss has been obtained at a temperature of about 800^0C this may be due to any structural change at high temperature.

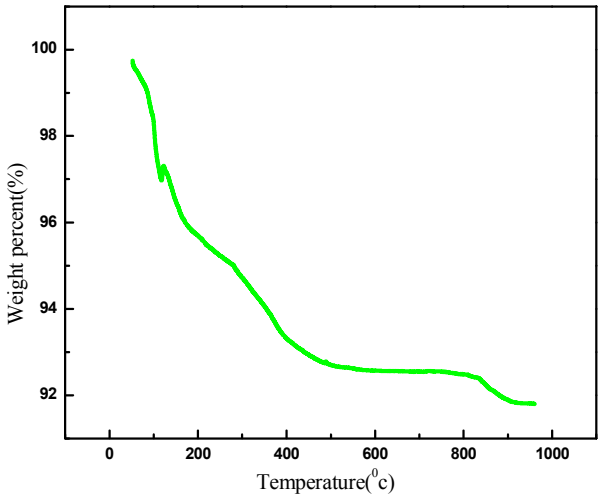

Figure 4.22: TGA of pure ZnO

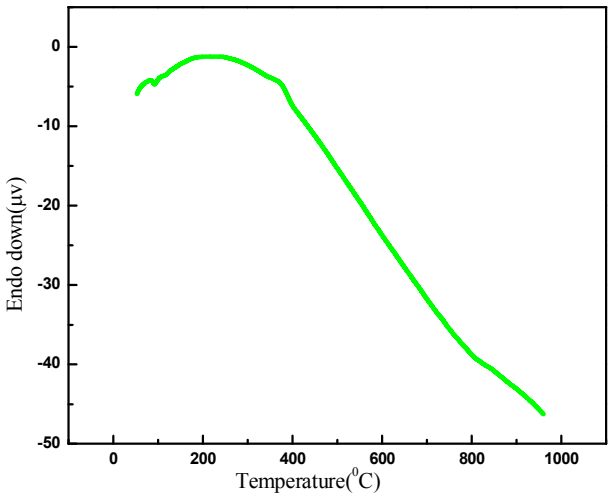

Figure 4.23: DTA of pure ZnO

4.4.2 Differential Thermal Analysis of pure synthesized ZnO:

DTA spectrum of the synthesized ZnO is shown in the figure 4.23. No sharp peak was observed in the spectrum indicating that sample was crystalline in nature as prepared and there is no significant increase in the crystallinity of the sample with rise in temperature.

4.5 Morphological Analysis

The surface morphology of the synthesized samples have been investigated using Scanning Electron Microscope at 10,000X.

4.5.1 Morphological analysis for pure ZnO:

SEM micrograph obtained for pure as prepared and calcined ZnO (at 500^0C for 2 hrs) is shown in the figure 4.24 (a) and 4.24 (b).

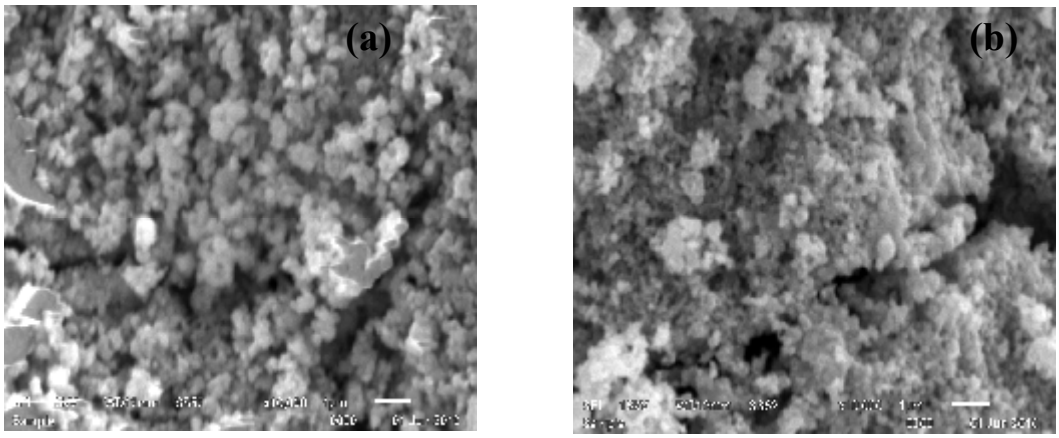

Figure 4.24: SEM micrograph of pure ZnO (a)as preapered (b)after calcination at 500^0C

From the figure, it is quite evident that no definite morphology has been observed in the sample. It seems that the spherical particles were agglomerated and form clusters. As the particle size calculated from the XRD analysis is in nano range, we are not getting any exact information about the surface morpholgy of the sample at 10,000X. The morphology observed in the samples is not showing any hard grains , which gives the idea that size of the particle is small and further needs to be characterized by Transmission electron microscopy (TEM) to obtain exact morphology and size of the particles.

4.5.2 Morphological analysis for Co (5 at%) doped ZnO:

Figure 4.25 shows the SEM micrograph of Co (5 at%) doped ZnO.

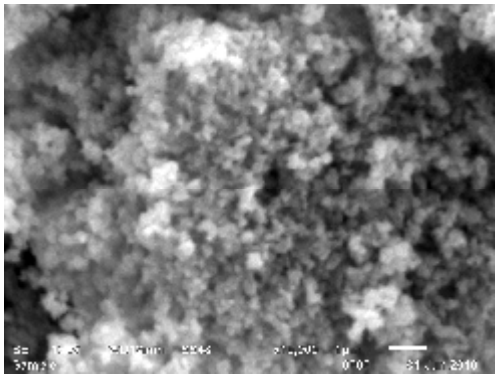

Figure 4.25: SEM micrograph for Co-doped ZnO

It has been found that the micrograph of Co-doped sample is also not giving any useful information at this magnification (10,000X). Only the clumps of spherical particles are observed.

4.6 Magnetic Measurements

Magnetic measurements have been performed for pure and doped ZnO (with transition metals (Ni, Co, Mn- 5 at%)) using SQUID (Quantum Design's MPMS XL7) magnetometer at 300K.For this study, samples have been calcined at 500^0C for 2 hours, in order to remove moisture and carbonaceous compounds.

4.6.1 Magnetic properties of pure ZnO:

Magnetization (M) versus magnetic Field (H) hysteresis loop obtained for pure ZnO is shown in the figure 4.26.

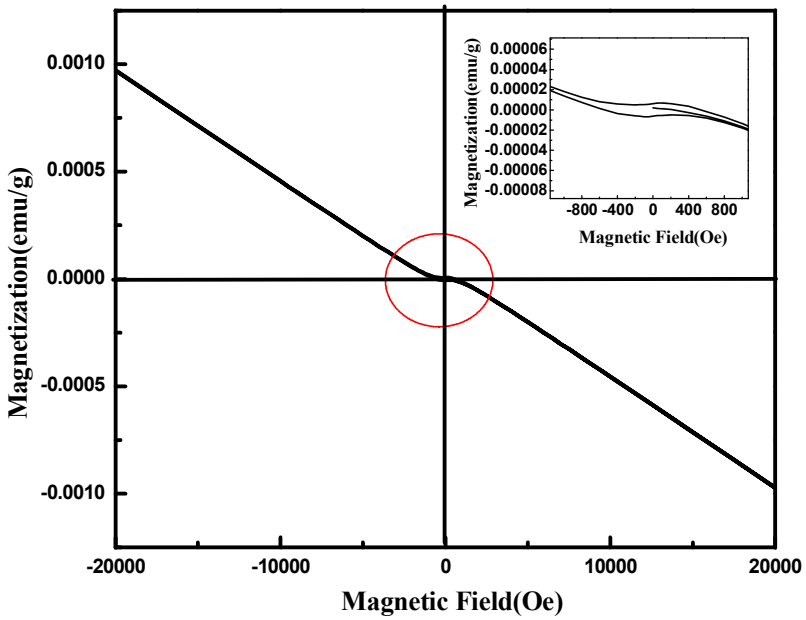

Figure 4.26: Hysterisis loop for pure ZnO

It is clear from the magnetization curve that the synthesized ZnO sample exhibits the diamagnetic character as bulk ZnO does. However at very low field values, there is observed a ferromagnetic like contribution as shown in the inset. Thus the synthesized sample is partly diamagnetic and partly ferromagnetic in nature.

After subtracting the diamagnetic contribution from the magnetization data[59], the ferromagnetic like hysteresis is obtained, as shown in the figure 4.27. Thus, the synthesized

pure ZnO shows ferromagnetic behaviour with remanence value 5.93×10^{-6} emu/g and coercive field 74.48 Oe, however these values are very much smaller than those have been reported in literature[49].

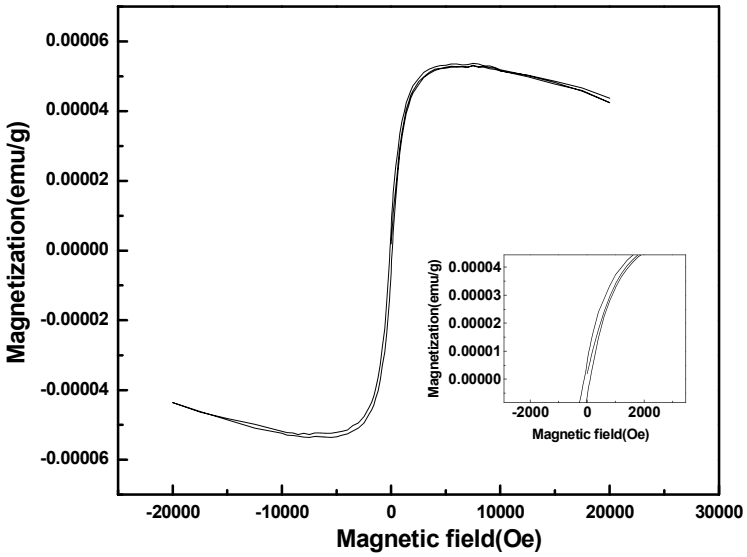

Figure 4.27: Hysteresis loop for pure ZnO after subtracting diamagnetic contribution[59]

The origin of ferromagnetism in ZnO nanoparticles is the exchange interactions between localized electron spin moments, resulting from the oxygen vacancies at the surfaces of the nanoparticles.

4.6.2 Magnetic properties of Ni-doped ZnO:

Hysteresis loop obtained for ZnO doped with Ni (5 at%). is shown in the figure 4.28.

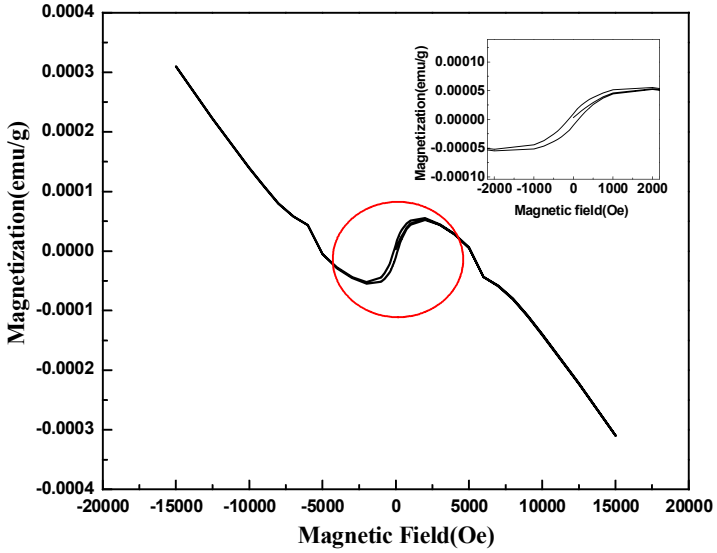

Figure 4.28: Hysteresis loop for Ni-doped ZnO

It was found that the Ni-doped ZnO exhibits a mixture of diamagnetic and ferromagnetic character, later being more dominant. After subtracting the diamagnetic contribution from the data, ferromagnetism like hysteresis plot has been obtained as shown in the figure 4.29.

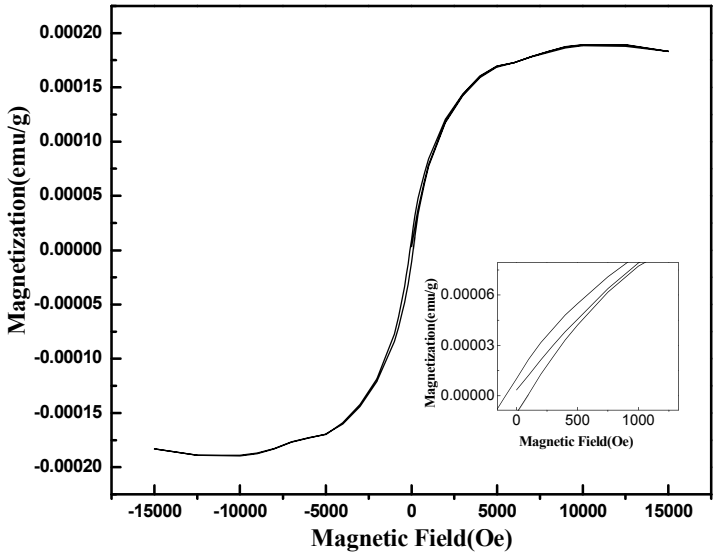

Fig 4.29: Hysteresis loop for Ni-doped ZnO after subtracting diamagnetic Contribution

The values of the remenance and coericivity are found to be 1.016×10^{-5} emu/g and 106.8462 Oe respectively. It is clear that with the incorporation of Ni^{2+} ions, the

ferromagnetic nature has been increased and hence the M_r and H_c values also increase. In literature, the ferromagnetism in Ni-doped ZnO has been explained due to the presence of secondary phases. But there is no possibility of such phases in our sample, as revealed by XRD analysis. In our case, the observed RT-FM can be ascribed due to the exchange interaction between free carriers and the localized Ni^{2+} ions occupied in the Zn sites. Such magnetic behaviour in nickel doped samples has been observed for the first time to the best of our knowledge and literature review.

4.6.3. Magnetic properties of Co-doped ZnO:

Magnetization (M) versus Magnetic Field (H) plot obtained for Co-doped ZnO (5 at%) is shown in the figure 4.30.

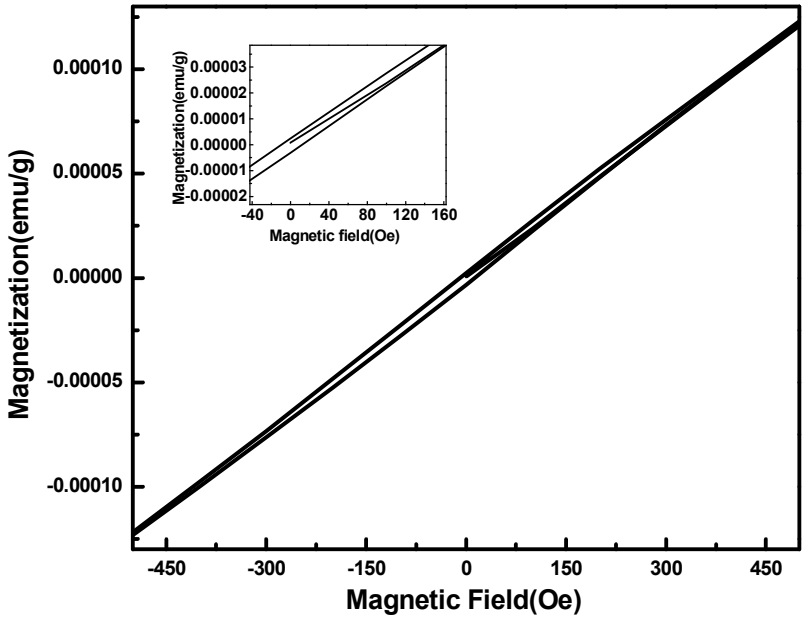

Figure 4.30: Hysteresis loop for Co-doped ZnO

It is clear from the plot that pure ferromagnetism has been achieved in ZnO with the substitution of Co (5 at%). The values of remenance and coericivity have been found to be 1.8941×10^{-6} emu/g and 7.5355 Oe respectively. The small coericivity and the small area under the hystresis loop characterizes theses materials as soft ferromagnets.

In case of Co-doped samples, the oxygen vacancies have little effect on the magnetic couplings because the 3d states lie high in the 2p (O)-4s (Zn) gap and induced donor state is too deep to significantly affect the occupancy of the extended TM (Transition metal)

levels. In contrast, both Zn interstitials and Zn vacancies change the occupancy of extended TM levels. As shallow donors, these Zn_i ions tend to form bound magnetic polarons in the lattice, where ferromagnetic couplings between the Co ions are mediated by the donor electrons from Zn_i ions. Only with the Zn_i increasing above a certain percolation threshold, these BMP (bound magnetic polarons) would overlap with each other, giving rise to a long range ferromagnetism. Such a mechanism for ferromagnetism is referred to as the impurity band exchange model.

4.6.4 Magnetic properties of Mn doped ZnO:

Figure 4.31 shows the hysteresis plot obtained for ZnO doped with Mn (5 at%). The curve clearly reveals the room temperature ferromagnetic ordering in the sample The remenant magnetization and coericivity estimated comes out to be 6.23196×10^{-6} emu/g and 20.472 Oe respectively.

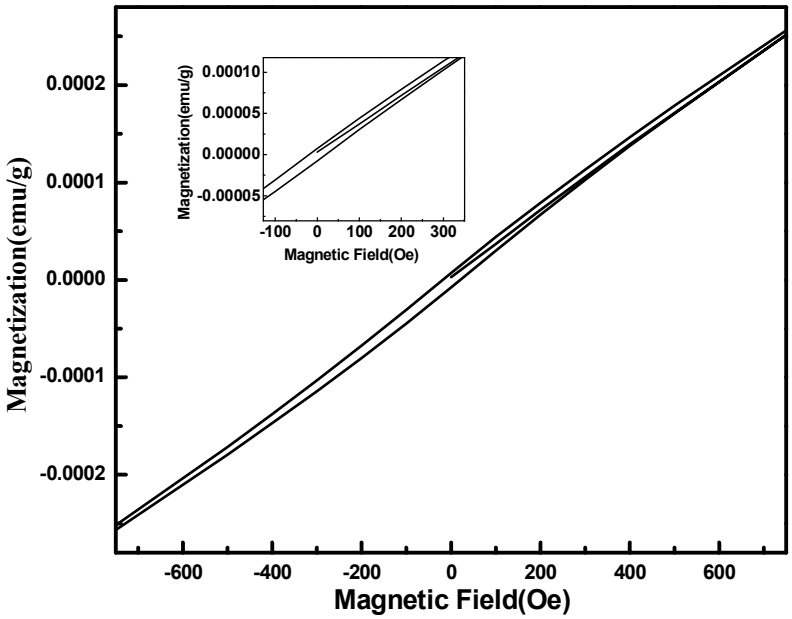

Figure 4.31: Hysteresis loop for Mn-doped Zn

As the origin of ferromagnetism, the possibility of secondary phase can be ruled out. Since in our case, XRD patterns confirm the formation of single phase only. As in the case of Co-doping, here also oxygen vacancies have a little effect on the magnetic couplings and the ferromagnetic state is stabilized by the presence of Zn interstitials and Zn vacancies. Thus impurity band exchange model is responsible for the ferromagnetism in this case also

The magnetic characteristics of all the synthesized samples has been summarized in the following table 4.8.

Table 4.8 Magnetic characteristics of synthesized samples:

Sample	Magnetic character	M_r (emu/g)	H_c (Oe)
Pure ZnO	Diamagnetic+ ferromagnetic	5.93×10^{-6}	74.48
ZnO:Ni-5%	Diamagnetic+ ferromagnetic	1.016×10^{-5}	106.8462
ZnO:Co-5%	Ferromagnetic	1.8941×10^{-6}	7.5355
ZnO:Mn-5%	Ferromagnetic	6.23196×10^{-6}	20.472

It is clear from the above table that, the M_r and H_c values are the highest for Ni-doped ZnO. This is because of the decrease in the lattice constants of Ni-doped samples, which induces the contraction in the lattice As the magnetic ions are more closely packed in this case, the spin dependent interaction between localized spins and holes in the valence band becomes stronger, and leads to a large ferromagnetic coupling.

Also, the Mn-doped ZnO has larger Remenance and coericivity values as compared to that in Co-doped ZnO. This is due to the fact that the Mn^{2+} has five unpaired electrons in its 3d shell ($3d^5$), whereas Co^{2+} has only three unpaired electrons ($3d^7$). The more number of unpaired electrons provides more localized spins in the system and hence strong magnetic coupling.

CONCLUSIONS

- We have successfully synthesized single phase ZnO by using Co-precipitation method in basic medium having particle size about 7-26 nm. In addition, the transition metals (Ni, Co and Mn) have also been doped upto 5%. Further, to study the effect of codopant, Co as well Mn-doped ZnO have been codoped with Antimony. All the samples have been found to exhibit wurtzite hexagonal crystal structure. The lattice constants for all the samples have also been calculated, which found to be decreased in Ni-doped system though in case of Co and Mn , no significant variation was seen.

- Fourier Transform Infrared spectroscopy also confirms the formation ZnO showing peak around 450cm^{-1}, which are in good agreement with XRD data.

- In the Electronic absorption spectra, the absorption wavelength (362.0168 nm) for the synthesized ZnO has been found to be blue shifted by 18 nm as compared to the bulk (380 nm) and hence the band gap has been increased. Also it has been found that the band gap increases with increase in Co-concentrations whereas it gets declined towards lower values with the increase in Ni and Mn content.

- Thermal analysis presents the stability of the phase upto higher temperatures.

- The hysteresis loop for pure ZnO has been found to indicate diamagnetic character as does bulk ZnO. Whereas at lower field values, it has been found to exhibit ferromagnetic behaviour. With the doping of Nickel, a mixture of diamagnetic and ferromagnetic behaviour has been observed, the later being more dominant. Although the pure ferromagnetism has been observed with the doping of cobalt and manganese. We have seen such ferromagnetic behaviour in Ni and Mn doped (5 at%) ZnO first time (As no report of such behaviour has been found in the literature.)

.

Future Perspective:

In the field of spintronics, the fabrication of devices, where both of the charge and spin functionalities of the carrier were combined, will be capable of integrating the electronics, magnetism, and optical functionalities in single material. These devices could revolutionize the technology by providing new device designs and architectures that could potentially boost performance, reduce power consumption, and introduce new features e.g. instantaneous boot up and data retention in the power-down state. Thus, Spintronics devices have the potential to revolutionize the IT industry as did the development of transistor 50 years ago. In future, our effort shall be to explore our study in this field to make efficient material with enhanced properties for device applications

References:

[1] http://www.nanotech-now.com/spintronics.html.

[2] "Introduction to spintronics" by Bandyopadhyay Supriyo Cahay Marc.

[3] http://www.research.ibm.com/research/gmr.html.

[4] H. Ohno. Science **281**, 951 (1998).

[5] T. Fukumura, Z.Jin, M. Kawasaki, T.Shono, T. Hasegawa, S. Koshihara, H. Koinuma, Appl. Phys. Lett. **78**, 958 (2001).

[6] Ü. Özgür, Ya. I. Alivov, C. Liu, A. Teke, M. A. Reshchikov, S. Dogan, V. Avrutin, S.-J. Cho, and H. Morkoç. J. Appl. Phys. **98**, 041301 (2005).

[7] P. Sharma, K. Sreenivas, and K. V. Rao, J. Appl. Phys**. 93**, 3963 (2003).

[8] Z. Jin, T. Fukumura, M. Kawasaki, K. Ando, H. Saito, T. Sekiguchi, Y. Z. Yoo,M. Murakami, Y. Matsumoto, T. Hasegawa Appl. Phys. Lett. **78** 3824(2001).

[9] Y. Imai, A. Watanabe and I. Shimono, J. Mater. Sci. **14,** 149 (2003).

[10] X.P. Shou, S.Y. Ming, S.C. Shu, P.H. Bin, Chin. Phys. Lett. **18**, 1252 (2001).

[11] F.A. Kroger, The Chemistry of Imperfect Crystals, North-Holland Publishing Company, Amsterdam, **691** (1964).

[12] W. Göpel, J. Pollmann, I. Ivanov and B. Reihl, Phys. Rev. B **26** 3144-3150(1982).

[13] T. Dietl, H.Ohno, F. Matsukura, J. Cibert, and D. Ferrand. *Science* **287**, 1019 (2000).

[14] K. Sato, H. Katayama-Yoshida, Jpn. J. Appl. Phys. **39**, L555 (2000).

[15] K. Sato, H. Katayama-Yoshida, Semicond. Sci. Technol. **17**, 367 (2002).

[16] C. Zener.Phys. Rev. **81**, 440 (1951).

[17] Subhash Thota, Titas Dutta and Jitendra Kumar J. Phys.: Condens. Matter **18,** 2473–2486 (2006).

[18] M.A. Ruderman and C. Kittel. Phys. Rev. **96**, 99 (1954).

[19] T. Kasuya, Prog. Theor. Phys. **16**, 45 (1956).

[20] K. Yosida. Phys. Rev. **106**, 893 (1957).

[21] T. Dietl, A. Haury, Y. Merle d'Aubigné. Phys. Rev. B **55**, R3347 (1997).

[22] H.Akai. Phys. Rev. Lett. **81**, 3002 (1998).

[23] C. Liu, f. Yun, h. Morkoc, journal of materials science: materials in electronics **16**

555– 597(2005)

[24] M. N. Baibich, J. M. Broto, A. Fert, F. Nguyen Van Dau, F. Petroff, P. Etienne, G. Creuzet, A. Friederich, and J. Chazelas. Phys. Rev. Lett. **61**, 2472 (1988).

[25] S. A. Wolf, D. D. Awschalom, R. A. Buhrman, J. M. Daughton, S. von Molnár, M. L. Roukes, A. Y. Chtchelkanova, and D. M. Treger.Science **294**, 1488(2001).

[26] S. Datta, and B. Das. Appl. Phys. Lett. **56,** 665 (1990).

[27] Yu. Bychkov, E.L. Rashba. J. Phys. C **17**, 6093 (1984).

[28] K. Sato, and H. Katayama-Yoshida, Mat. Res. Soc. Symp. Proc. **666** (2001) .

[29] T. Kasuya, and A. Yanase, Rev. Mod. Phys. **40**, 684 (1968).

[30] P. M. Amirtharaj, F. H. Pollak and J. K. Furdyna, Solid-State Commun. **39**, 35 (1981).

[31] H. Munekata, H. Ohno, S. von Molnar, A. Segmuller, L.L. Chang, and L. Esaki, Phys. Rev. Lett. **63**, 1849 (1989).

[32] H. Ohno, H. Munekata, T. Penney, S. von Molnar, and L.L. Change, Phys Rev.Lett. **67**, 2664 (1992).

[33] H. Ohno, A. Shen, F. Matsukura, A. Oiwa, A. Endo, S. Katsumoto, and Y. Iye., Appl.Phys. Lett. **69**, 363 (1996).

[34] A.M. Nazmul, S. Sugahara, and M. Tanaka, Phys Rev. B **67**, 241308 (2003).

[35] T. Dietl, H.Ohno, F. Matsukura, J. Cibert, and D. Ferrand, Science **287**, 101(2000).

[36] C. Zener, Phys. Rev. **81**, 440 (1951) .

[37] M. L. Reed, N. A. El-Masry, H. H. Stadelmaier, M. K. Ritums, M. J. Reed, C. A.Parker, J. C. Roberts, and S. M. Bedair, Appl. Phys. Lett. **79**, 3473 (2001).

[38] K. Ueda, H. Tabata, and T. Kawai., Appl. Phys. Lett. **79**, 988 (2001).

[39] T Mizokawa, T. Nambu, A Fujimori, T Fukumura and M.Kawasaki, Physical Review B, **65**, 085209(2002).

[40] A.S.Risbud, N.A.Spaldin, Z.Q.Chen, S.Stemmer, and Ram Seshadri , Physical Review B **68**, 205202 (2003).

[41] D. P. Nortona) and S. J. Pearton, A. F. Hebard and N. Theodoropoulou, L. A. Boatner, R. G. Wilson, Appl. Phys. Let. **82**, NUMBER 2 (2003).

[42] Parmanand Sharma, Amita Gupta, K.V. Rao, Frank J. Owens, Renu Sharma, Rajeev Ahuja, J. M. Osorio Guillen, Börje Johansson and G. A. Gehring , Nat. Mater **984** (2003).

[43] B. B. Li, X.Q. Xiu, R. Zhang, Z. L. Xie, Y. Chen, Y. Shi, P. Han, Y. D. Zheng, IEEE (2004).

[44] Jung H. Park, Min G. Kim, Hyun M. Jang, and Sangwoo Ryu, Appl. Phys.Lett. **84,** NUMBER 8(2004).

[45] C. N. R. Rao and F. L. Deepak, J.mater chem. **15**,573-578 (2005) .

[46] Nguyen Hoa Hong and Virginie Brize, Appl. Phys. Let. **86**,082505 (2005).

[47] Kevin R. Kittilstved, Nick S. Norberg, and Daniel R. Gamelin, Physical review Letters **94,** 147209 (2005).

[48] Marcel H. F. Sluiter, Y. Kawazoe, Parmanand Sharma, A. Inoue, A. R. Raju, C. Rout, and U.V. Waghmare, Physical Review Letters **94**, 187204 (2005).

[49] A. Sundaresan, R. Bhargavi, N. Rangarajan, U. Siddesh and C. N. R. Rao , Physical Review B **74**, 161306(R) (2006).

[50] Kanwal Preet Bhatti, Shankhamala Kundu, Sujeet Chaudhary,Subhash C Kashyap and Dinesh K Pandya J. Phys. D: Appl. Phys. **39** 4909–4914 (2006) .

[51] X.C.Liu, E.W.Shi, Z.Z.Chen, H.W.Zhang, B.Xiao and L.X.Song, Applied physics letters **88**, 252503 (2006).

[52] A. Manivannan, P. Dutta, G. Glaspell, and M. S. Seehra, Journal Of Applied Physics **99**, 08M110 (2006).

[53] Sasanka Deka and P. A. Joy, Appl. Phys. Lett. **89**, 032508 (2006).

[54] O D Jayakumar, H G Salunke, R MKadam, Manoj Mohapatra, G Yaswant and S K Kulshreshtha, Nanotechnology **17** 1278–1285 (2006) .

[55] V. K. Sharma, R. Xalxo, and G. D. Varma, Cryst. Res. Technol. **42**,34 – 38 (2007).

[56] M.Ivill and S.J.Pearton, Y.W.Heo,J.Kelly and A.F.Hebard, D.P.Norton, Journal of Applied Physics **101**, 123909 (2007).

[57] Stephen j.Pearton, fellow, IEEE, david P.Norton, Matt P.Ivill, Art F. Hebard, john M.Zavada, Weimin M.Chen, and Irina A. Buyanova, IEEE Transactions On Electron Devices VOL. **54**, NO. 5.(2007).

[58] Kanwal Preet Bhatti, Sujeet Chaudhary,a_ Dinesh K. Pandya, and Subhash C. Kashyap Journal Of Applied Physics **101**, 103919 (2007).

[59] M. A. Garcia, J. M. Merino, E. Ferna´ndez Pinel, A. Quesada, J. de la Venta, M. L. Ruı´z Gonza´lez, G. R. Castro, P. Crespo, J. Llopis, J. M. Gonza´lez-Calbet, and A.Hernando, Nanoletters VOL. **7**,No. 6 1489-1494 (2007).

[60] Y. He, Parmanand Sharma, Krishanu Biswas, E. Z. Liu, Naofumi Ohtsu,A. Inoue, Y. Inada, M. Nomura, J. S. Tse, S. Yin, Physical Review B **78**, 155202 (2008).

[61] Daqiang Gao, Zhaohui Zhang, Junli Fu, yan Xu, Jing Qi, and Desheng Xue. Journel of Applied Physics **105**, 113928 (2009).

[62] Michael Snure, Dhananjay Kumar, and Ashutosh Tiwari, Appl. Phys.Lett. **94,** 012510 (2009).

[63] Tongfei Shi, Zhenguo Xiao, Zhijun Yin, Xinhua Li, Yuqi Wang, Hongtao He, Jiannong Wang, Wenshen Yan, Appl. Phys. Lett **96**,211905 (2010).

[64] X.J.Ye, C.S.Liu, H.A.Song, C.t.au, Y.W.Du , Physics letters A **374** 496-500(2010).

[65] Xiao-Lin Wang, Shi Xue Dou and Chao Zhang, NPG Asia Mater**. 2**(1) 31–38 (2010).